Modulation of Semiconductor Photoluminescence with Intense Terahertz Pulses

by

David N. Purschke

A thesis submitted in partial fulfillment of the requirements for the degree of

Master of Science

Department of Physics
University of Alberta

Abstract

Over the last 5 years, tilted pulse-front terahertz (THz) generation has opened the door to new studies of nonlinear dynamics in a variety of materials. With access to strong electric fields that turn on and off over picosecond timescales exciting new possibilities exist to control light-matter interaction. We have developed a new intense THz pulse source, with a peak electric field of 230 kV/cm for exploring nonlinear dynamics in semiconductors.

Here, we study the effects of THz pulses on semiconductor photoluminescence (PL). When a femtosecond optical and single-cycle intense THz pulse are simultaneously incident on a direct-gap semiconductor, the THz pulse enhances high energy and quenches low energy PL. However, with time delays larger than 1 ps, no modulation of the PL occurs.

We have systematically studied the THz-pulse-induced change in PL (THz-ΔPL) over a wide range of THz energies and photoexcitation densities in gallium arsenide (GaAs) and indium phosphide (InP) to help understand the mechanism. In most cases, the quenching dominates and there is integrated PL quenching (PLQ). With increasing photoexcited carrier density, the fractional quenching decreases, while the enhancement increases, and less integrated modulation occurs. At high excitation density, by changing

the temporal profile of the photoexcitation pulse, the enhancment can be made to dominate and there is integrated PL enhancement (PLE).

The origin of this behaviour has to do with the redistribution of carriers in phase space by the strong electric field of the THz pulse. In real space, oppositely charged electrons and holes are spatially separated. In momentum space, hot electrons scatter to satellite valleys, increasing the rise-time of the PL, slowing carrier diffusion, and releasing a large number of high wavevector phonons.

Despite our understanding of these processes, a precise description of the THz-ΔPL is still not completely clear. Possible explanations for these effects are discussed, including suppression of stimulated emission, enhanced surface recombination, and non-radiative recombination involving intervalley phonons.

Preface

I herewith declare that I have produced this paper without the prohibited assistance of third parties and without making use of aids other than those specified; notions taken over directly or indirectly from other sources have been identified as such.

The thesis work was conducted from September 2014 to August 2016 under the supervision of Frank Hegmann at the University of Alberta.

Acknowledgements

Grad school is a lot like riding a roller coaster built by a person who had no idea what they were doing. It just sounded like fun, so they gave it a shot. In this case, that person is you. You started building your own roller coaster the day you decided to go to grad school. My own roller coaster has had many ups and downs. There will be many more to come, as I begin my PhD studies in just two weeks. What I've learned so far is a little bit about building roller coasters, and a lot about how important it is to have help doing it.

With that, I would like to start by thanking my supervisor, Dr. Frank Hegmann. You've been there for me more times than I can count. It goes without saying that I would not have gotten to this point without your help and guidance. I would like to thank our former research associate, Dr. Lyuba Titova. My first eight months in the lab were under your guidance and I will not forget what I learned from you about both terahertz pulses, and life.

I would like to thank my Committee members, Dr. Rick Sydora and Dr. Joseph Maciejko, who have provided me with valuable advice. I would especially like to thank Joseph whos door has always been open when I've had questions. I would like to thank Greg Popowich, and Beipei Shi for technical support. I would like to thank Dr. Frank Marsiglio, and Dr. Lindsay LeBlanc for their helpful discussions.

I would like to thank my current and former lab mates Vedran Jelic, Mary Narreto, Peter Ngyuen, Cameron Hough, Charles Jensen, Glenda de los

Reyes, Ayesheshim Ayesheshim, Zhenyou Wang, Christopher Rathje, Alexander Bourgund, and William Morrish. I would especially like to thank Mary Narreto who edited my entire thesis in one day, for which I am very grateful. I would like to thank all current and former undergraduate students who have worked with me: Andrew Longman, Ketty Na, Haille Sharum, Christopher Mannes, Kameron Palmer, and Daniel Mildenberger. I would also like to thank Daniel for providing the FROG trace that is in my thesis.

I would like to thank my former roommates Scott and Jenn, and my current roommate Andrew, all of whom I leaned on for support during times of stress. I would like to thank all of my friends who helped make me who I am. I would like to thank my intramurals sports teams, as bad as it sounds there is no better stress relief than hitting a layup, a spike, or tossing a hammer for a point.

I would like to acknowledge the thousands of individuals who have coded for the LaTeX project for free.

And finally, I would like to thank the people who I lean on the most. My girlfriend Tatiana, who has been more supportive and understand than I could hope for. Tata, I'm lucky to have you. My brother Andrew, and his wife Carrie, and my grandparents, Fran, Norm, and Irene. Most of all, I would like to thank my parents Garry and Eunice for their support. Throughout it all, you have not only allowed me to find my own way in life, but you have helped facilitate it. I am forever in your debt.

Contents

List of Figures

List of Tables

Acronyms

APD avalanche photodiode. 26, 45

BBO beta barium borate. 30, 38

CCD charge-coupled device. 26, 31, 45

CdTe cadmium telluride. 48, 71

CW continuous wave. 28

EM electromagnetic. 3

EO electro-optic. ix, 26, 34, 37, 38, 41, 43–45

FFT fast fourier transform. 43, 44

FROG Frequency Resolved Optical Gating. 31

fs 1 femtosecond = 10^{-15} s. 2, 31

FWHM full-width half-max. 23, 30, 31

GaAs gallium arsenide. ii, 3, 4, 26, 45, 48–51, 53, 62, 68, 74

GaP gallium phosphide. 34

GVD group velocity dispersion. 28, 41

hh heavy hole. 10

InP indium phosphide. ii, x, 4, 26, 49–51, 53, 62, 63, 68, 71, 74

lh light hole. 10

LN lithium niobate. 4, 26, 33, 34, 39, 40

LO longitudinal optical. 12, 51, 53

NIR near infrared. 26, 50

nm 1 nanometer = 10^{-9} m. 2

OR optical rectification. 26

PL photoluminescence. ii, x, 4, 26, 27, 47–49, 51, 53, 55, 56, 58, 62, 63

PLE photoluminescence enhancement. 4, 49, 53, 57, 61, 62

PLQ photoluminescence quenching. 4, 48, 49, 53, 55, 57, 62, 69

SHG second harmonic generation. 38

SO split-off. 10, 11, 51

SPM self-phase modulation. 41

THz 1 terahertz = 10^{12} Hz. ii, x, 2–4, 7, 22, 26, 27, 32–34, 39–41, 43–49, 51, 53–56, 60, 62, 63, 68–70, 74

Ti:Sapphire titanium doped sapphire. 2, 3, 26, 28

TO transverse optical. 12

TPFP tilted pulse front pumping. 33, 44

1

Introduction

Over the last several decades, our ability to predict and control light-matter interactions has proceeded hand in hand with the development of novel light sources. This is highlighted with the first demonstration of the optical laser in 1960 (1), giving researchers on-demand access to intense, coherent light. This led to the development of the entirely new field of nonlinear optics, where materials are driven far enough from equilibrium that their optical properties are modulated by the light field itself(2).

In the following decades, laser technology expanded into new regimes of wavelength, pulse duration, and intensity using novel gain media, and mode-locking techniques. Today, titanium doped sapphire (Ti:Sapphire) oscillators operating near 800 nm are used to generate pulses which switch on and off in under 10 fs, and laser amplifiers can output pulses where the electric field is strong enough to tear electrons away from their host molecules in air(3).

On one frontier, cutting edge research in ultrafast science is pushing pulse durations to the attosecond (10^{-18} s) regime(4). However, rather than push in the direction of faster and faster pulses, we take a different approach and instead attempt to combine ultrafast and nonlinear in a new region of the electromagnetic spectrum. We are studying how intense, transient electromagnetic fields at THz frequencies interact with semiconductors, redistributing carriers in phase space(5).

Located between the microwave and infrared portion of the electromagnetic spectrum is the THz regime, as seen in fig. 1.1. This region was historically known as the THz gap, as neither conventional photonics nor electronics technology are efficient at these freqeuncies. In the last two decades, a range of techniques relying almost exclusively on nonlinear optics were developed to bridge this gap. The field has grown to the point where the THz region should no longer be considered a gap(6). Today researchers are even adapting the THz toolkit to new regions of the spectrum, even as far as the near-infrared region(7).

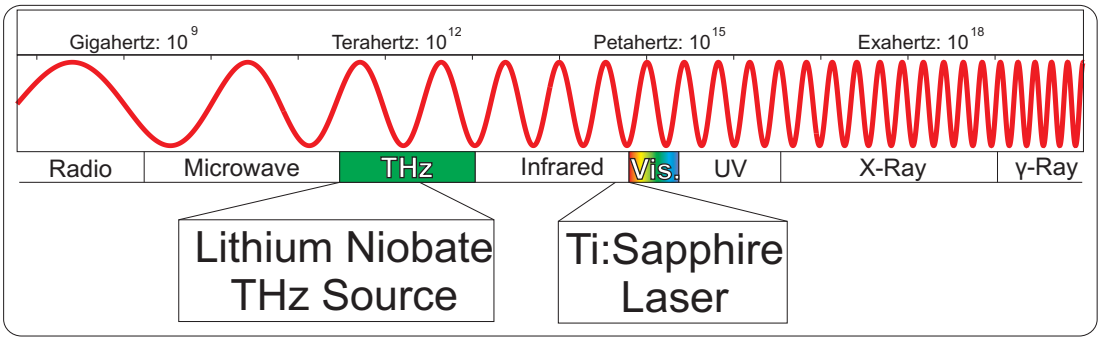

Figure 1.1: Electromagnetic Spectrum - The electromagnetic (EM) spectrum and its various regions. The THz region is defined as light with frequencies between 0.1 and 10 THz, located between the microwave and infrared regions. We generate intense THz pulses with frequencies from 0.1 to 2.5 THz using high power femtosecond pulses from a Ti:Sapphire laser, which operates just outide the visible part of the spectrum.

As a spectroscopic tool, THz pulses have resulted in many interesting breakthroughs in our understanding of light-matter interactions. Some of the pioneering work in the field came as far back as 1987 when Nuss *et al.* studied the transient mobility of electrons in GaAs after ultrafast excitation(8). This was the first evidence that intervalley scattering strongly affects relaxation dynamics after ultrafast excitation. For the first time, researchers had the ability to measure conductivity on picosecond timescales.

Since then, THz science has provided many other unique insights into the physics of semiconductors. To highlight just a few of the results, Huber *et al.* studied the quantum kinetic build up of correlations in a photoexcited plasma in GaAs as the system moves from a bare charge to a plasmon-like response(9). Kaindl *et al.* discovered a unique regime of enhanced excitonic behaviour immediately after photoexcitation in

quantum wells(10). With new sources pushing to higher frequencies multi-THz pulses, with center frequencies of tens of THz, were shown to coherently drive carriers across the entire brillouin zone and emit high harmonics all the way to the visible part of the spectrum(11).

In the 0.1 to 3 THz regime, the recently developed technique of tilted-pulse-front pumping in lithium niobate (LN) has allowed for the generation of single cycle THz pulses capable of driving materials nonlinearly(12). The electric field measured directly in the time domain for one of these pulses is shown in fig. 1.2. A variety of new phenomenon have been discovered, such as self-amplitude modulation by intervalley scattering(13), coherent control of spin waves in antiferromagnetic materials(14), and light induced interband tunneling using field-enhancing plasmonic antennae(15). The unique nature of these sources, with huge electric fields that ramp on sub picosecond timescales, has led to many new applications in material control(16).

In this thesis, we study how intense THz pulses from LN sources can modulate PL in photoexcited direct-gap semiconductors (GaAs and InP). Light emission, a nanosecond timescale phenomenon, is typically the last step of carrier relaxation that follows carrier and lattice thermalization, which occurs over several picoseconds. These first few picoseconds are an extremely complex regime, with a variety of interactions affecting the dynamics. In a perfect direct gap semiconductor, almost all carriers recombine radiatively. However, in a real semiconductor there are imperfections, such as impurities and defects, which act as channels for non-radiative recombination.

We show that an intense THz pulse affects the amount of radiative vs non-radiative recombination, as well as the luminescence lineshape. A dynamic interplay between photoluminescence quenching (PLQ) near the gap, and photoluminescence enhancement (PLE) of hot luminescence occurs while varying the photoexcitation density. Perhaps most interestingly, when the optical pulse preceeds, or trails the excitation pulse by just 1 ps, no modulation of luminescence is observed. This behaviour seems to indicate that the THz pulse modifies the initial conditions of the decay, which effects the long term behaviour.

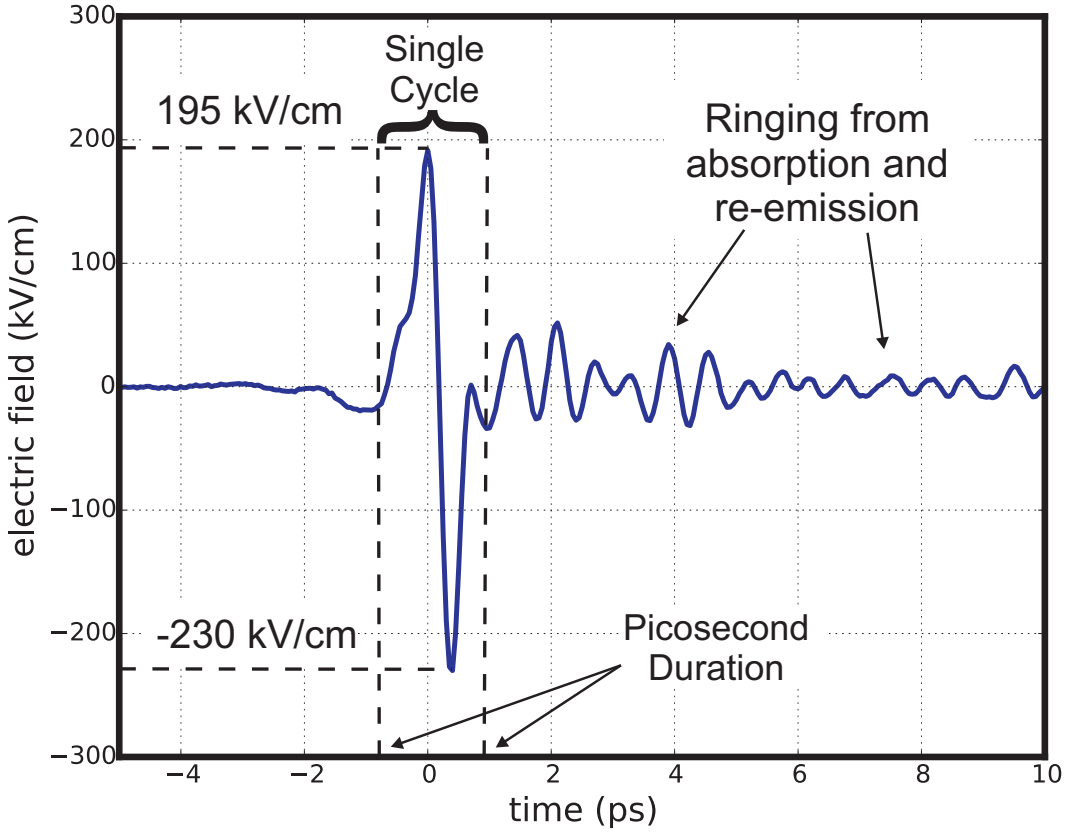

Figure 1.2: Terahertz Pulse - The electric field, measured in the time domain at the focus of the THz pulse. The pulse consists of a single cycle of the electromagnetic field, reaching a peak field of 230 kV/cm, while switching on and off in approximately a picosecond. The small oscillations after the peak of the THz pulse are due to absorption, and re-emission in the generation crystal, as well as water molecules in the air.

To see why, we must examine the dynamics of the first few picoseconds after excitation and see how THz pulses affect this process. In the next chapter, luminescence in semiconductors is presented in a general way in order to describe the interplay between radiative and non-radiative decay. We then introduce the tools used to describe optical interactions and high-field transport.

The experimental details are presented in chapter 3, including a short introduction to the mode-locked laser, and amplifier system. The design and construction of the intense THz pulse source is also discussed, including a guide to its alignment and operation. The methods for differential PL measurement are also presented. In particular,

the development of a novel method for parallel detection and simultaneous background subtraction.

Chapter 4 contains the experimental results on GaAs and InP. For GaAs, a broad range of excitation conditions were explored and presented. Qualitatively, the data was very similar in InP. However, several complementary studies were done in InP that were not possible in GaAs. Chapter 5 is a discussion of the results, offering several possible interpretations. Future experiments are proposed to elucidate the mechanism. Chapter 6 presents our conclusions and gives perspective on the relevance of this study.

2

Ultrafast Excitation and Relaxation of Semiconductors

The physics of semiconductors materials is very rich, having been studied from both an electronics and optics perspective for decades. In order to understand intense THz pulse interactions in photoexcited semiconductors both perspectives are required. This is especially true in order to understand the THz pulse modulation of luminescence where one must understand how high-field transport affects carrier distributions, and what happens on femtosecond timescales after optical excitation that makes this regime unique.

In general, luminescence involves the emission of light accompanying a transition between two quantum states. The transition rate from an initial to final state, W, is given by Fermi's golden rule,

$$W = \frac{2\pi}{\hbar} |\langle \psi_f | H' | \psi_i \rangle|^2 = \frac{2\pi}{\hbar} |M_{if}|^2, \tag{2.1}$$

where M_{if} is the matrix element of the perturbation hamiltonian, and *H'*, inducing the transition. Here we have assumed all states are unique and therefore did not include the density of final states as is typical. For the rate of spontaneous radiative decay, luminescence, we are interested in the dipole matrix element. At any given time, the emitted luminescence spectrum *I(E)* is proportional to this rate times the number of states separated by energy E, the joint density of states g(E),

$$I(E) \propto |M_{if}|^2 g(E) f_i (1 - f_f), \tag{2.2}$$

where we have also included the probability that the initial state is occupied, f_i, and the final state is unoccupied, $1 - f_f$. Therefore, if we know the energy structure and probability of occupancy f for each state, we can determine the rate and spectrum of radiative recombination. In practice, complete knowledge of the distribution is difficult to obtain, and photon re-absorption modifies the dynamics so that the problem is not so simple.

Additionally, carriers can recombine non-radiatively and transfer their excess energy to the lattice as heat. At any point in time, if there are N photoexcited carriers in the system the recombination rate can be expressed by adding the rates of radiative, k_R, and non-radiative, k_{NR}, recombination,

$$\frac{dN}{dt} = (k_R + k_{NR})\, N. \tag{2.3}$$

We have already seen how the radiative rate is a function of the distributions, energy structure, and matrix elements. The non-radiative rate, k_{NR}, is even more complicated, occuring through localized centers where the precise structure is unknown. Despite the complexity, we can write a general expression for the radiative efficiency, η_R, by considering the fraction of carriers that recombine radiatively at time t and integrating over the full decay,

$$\eta_R = \frac{1}{N_0} \int_{t_0}^{\infty} \frac{N(t)}{1 + \frac{k_{NR}(t)}{k_R(t)}} dt. \tag{2.4}$$

Here, we have divided by the initial carrier density, N_0, for normalization. The complexity of the rates is manifested in their time dependence, of which we have made no assumptions. Using this equation, we see that there are two ways to reduce the radiative efficiency: increase the non-radiative rate, k_{NR}, or decrease the radiative rate, k_R. The converse holds for enhanced radiative efficiency.

The purpose of this chapter is to 1) introduce the basic concepts of semiconductor physics, i.e, the electronic and vibrational structure, as well as defects or impurities,

2) Show how optically excited distributions evolve on ultrafast timescales and how this affects the luminescence spectrum, and 3) understand how strong electric fields drive carriers to large energies, modifying the distribution in phase space.

2.1 Semiconductor Physics

2.1.1 Crystal Lattice

GaAs and InP are both crystalline solids whose constituent atoms form a lattice with a regular repeating structure. Crystals are categorized based on their crystallographic point group, which defines the underlying symmetry of the lattice(17). Both GaAs and InP have zinceblende structure (class $\bar{4}$3m), consisting of two face centered cubic sub-lattices offset by a quarter of the unit cell in the (111) direction. The crystal symmetry places restrictions on the allowed optical transitions(18). The unit cell of the crystal contains four unique bonds, as shown in fig. 2.1 (a).

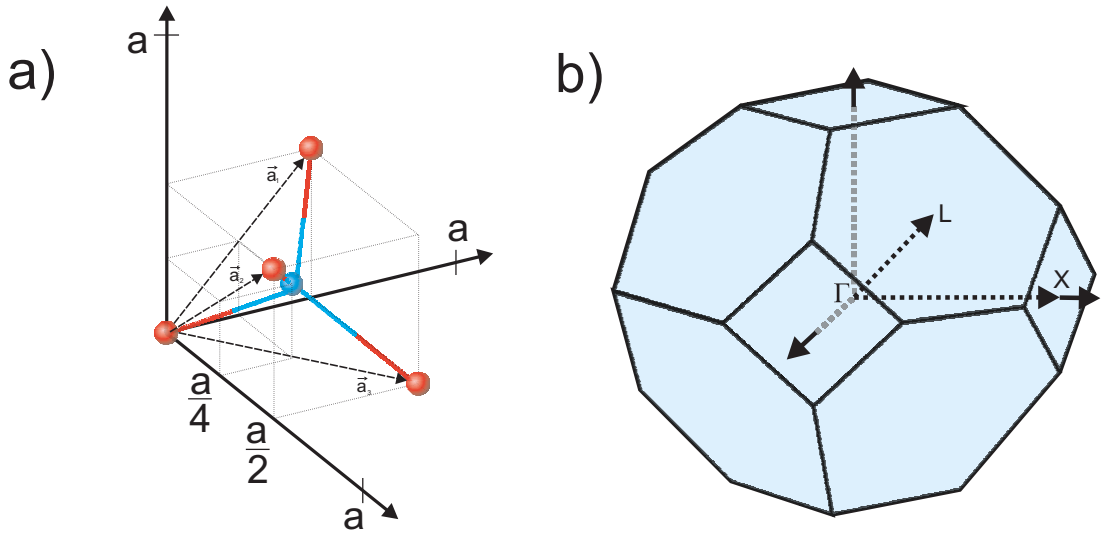

Figure 2.1: Zincblende properties - a) The structure of a zincblende crystal in real space, characterized by an fcc lattice with a two atom basis. The crystal structure is formed using combinations of this cell translated by integer multiples of the unit vectors, $\vec{a}_n$.The charges which contribute to bonding are shared asymmetrically between red and blue atoms, giving the bond a partially ionic character. b) The first Brillouin zone of a zincblende crystal in reciprocal space. There are three minima at high symmetry points: the Γ-valley (origin), L-valley (center of hexagonal faces), and X-valley (center of the square face).

The lattice periodicity points to an alternate description in Fourier space. A spatial

Fourier transform of the lattice results in a new lattice in what is known as reciprocal or k-space, where k is a wavevector. This space is critical to understanding optical interactions in semiconductors, as we will show later. In k-space, a special definition of the unit cell is chosen, called the Wigner-Seitz cell(19). It is defined, after choosing a lattice point as the origin, as the volume closer to the origin than any other lattice point. This cell is called the Brillouin zone, shown for a zincblende crystal in fig. 2.1 b), with the Γ, L, and X points of high symmetry labelled.

2.1.2 Electronic Structure

The energy levels resulting from level splitting when many identical atoms are brought close together form continuous bands. In a semiconductor, all bands are either full or empty at zero temperature. The gap between the highest valence (occupied), and lowest conduction (empty) bands is known as the band gap. Semiconductors are essentially transparent for photon energies below the gap, and opaque for photon energies above the gap.

Many different techniques exist for calculating band structure. Tight binding or $\mathbf{k} \cdot \mathbf{p}$ methods can give accurate band structures within several eV of the fermi level throughout the whole Brillouin zone, with a number of adjustable parameters(20, 21). More recently, ab-initio techniques have been developed which can calculate the full band structure accurately with zero adjustable parameters, although they are computationally expensive(22).

While real semiconductors have many bands, for optical excitation near the bandgap a four band model is sufficient. Here there are three valence bands, the light hole (lh), heavy hole (hh), and split-off (SO) hole bands, and one conduction band that are important. The relevant bands are shown schematically for a direct-gap semiconductor with zinc blende structure in fig. 2.2.

Near the band extrema, the dispersion is parabolic, and the energy as a function of wavevector can be written as,

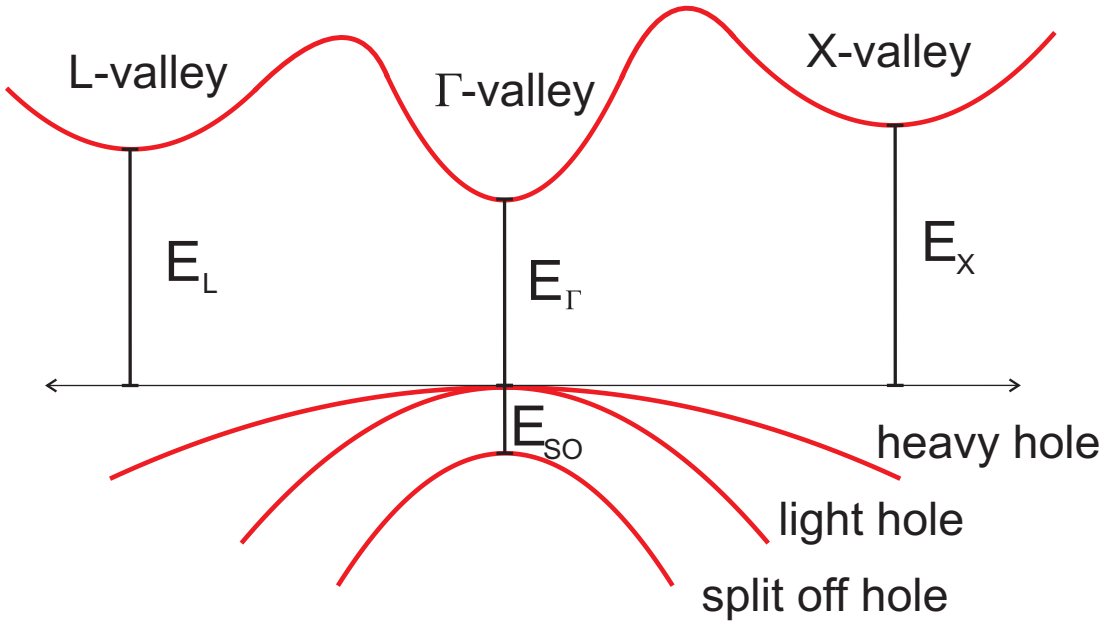

Figure 2.2: Zincblende Crystal Structure - The simplified band structure of a typical zincblende direct-gap semiconductor, showing only the bands relevant to the current study. There are three hole bands; the light, heavy, and split off hole. In the first conduction band, there are three minima; at the Γ, L, and X points in the Brillouin zone. Here, the valleys are connected smoothly, and the structure at the extrema with negative curvature is not accurate. There are 3 and 4 inequivalent X, and L valleys respectively, which can be seen from the geometry of the Brillouin zone in fig. 2.1.

$$E = \frac{\hbar^2 k^2}{2m^*}, \tag{2.5}$$

with an effective mass m^* determined by the curvature of the band. Non-parabolicity can be accounted for using a wavevector dependent effective mass. The joint density of states between any two bands, *g(E)* in eq. 2.2, can be found in the parabolic band approximation using the reduced mass between the two. Near the minimum, the Γ-valley of the conduction band is essentially isotropic, while the satellite valleys (X and L) are not. There are different longitudinal and transverse effective masses for the X and L valleys. In the semiconductors used in this work the longitudinal mass is larger.

The valence bands are more complicated as degeneracy leads to strong interactions between bands. The heavy and light holes are degenerate at k=0, while degeneracy is lifted by spin-orbit coupling for the SO band. The effective masses are anisotropic,

however the 9 independent parameters (m_{100}, m_{110}, and m_{111} for each of the hh, lh, and SO bands) can be reduced to 3 Luttinger parameters in zincblende crystals(23). In GaAs and InP, the anisotropy is not large.

2.1.3 Phonon Dispersion

The atoms which make up the lattice are free to oscillate about their equilibrium positions. The normal modes of vibration, similar to electron energies, can be conveniently described as a function of wavevector. With an infinite crystal, a continuous range of energies from the zone center to the zone edge is available for each degree of freedom in a unit cell. For a two-atom basis, as in zincblende, this results in 6 normal mode branches. Shown in fig. 2.3 is the normal mode dispersion along high symmetry directions, where degeneracy reduces the number of branches to only 4.

The energy of each mode is quantized, and the quanta of crystal lattice vibration is known as a phonon. Phonons with zero (nonzero) frequency at the zone center are called acoustic (optical) phonons. For both acoustic and optical phonons, there are longitudinal and transverse modes. In zincblende crystals, bonding has both covalent and ionic character, resulting in a charge asymmetry between sublattices. This results in a phonon with a dipole moment. The transverse optical (TO) phonon is therefore infrared active and can interact directly with light. Longitudinal optical (LO) phonons can interact with light indirectly by Raman (inelastic) scattering.

2.1.4 Thermal Excitations

At finite temperature, the assumption that all valence bands are full and conduction bands empty breaks down. For systems in thermal equilibrium, the statistics governing occupancy of excited electronic states can be described by the Fermi-Dirac distribution,

$$f(E) = \frac{1}{e^{\frac{(E \quad \epsilon_F)}{k_b T}} + 1}, \tag{2.6}$$

where k_b is the Boltzmann constant, T is the temperature, and ϵ_F is the Fermi level, or chemical potential. The number of electrons as a function of energy can be calculated by multiplying this function by the energy-dependent density of states. Electrons which

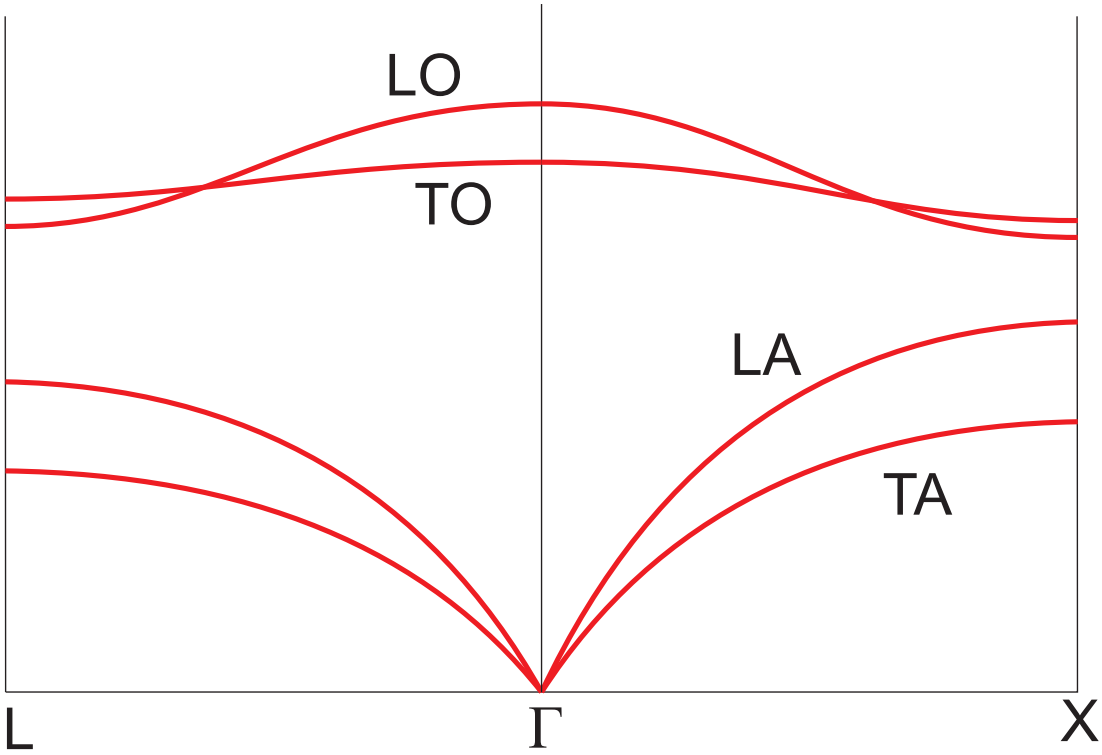

Figure 2.3: Zincblende Phonon Dispersion - Four non-degenerate branches of phonons exist along high symmetry directions in the Brillouin zone, corresponding to the 111 (L) and 100 (X) directions. LO (LA) refers to longitudinal optical (acoustic) phonons, and TO (TA) refers to transverse optical (acoustic) phonons. The acoustic branches have zero energy at the Γ-point, so electrons at the bottom of the band can both emit and absorb phonons. Optical phonons have non-zero energy, such that there is a threshold electron energy for emission.

occupy states in the conduction band leave behind a net positive charge in the valence band. This can be conveniently described as a hole, a particle which behaves like a positively charged electron.

In non-equilibrium situations, when no coherence exists in the system, the distributions of electrons and holes can be calculated using the eq. 2.6 with separate Fermi levels for electrons and holes that depend on the level of excitation. When these quasi-Fermi levels are in the conduction (valence) band for electrons (holes), there is a population inversion, and stimulated emission of radiation can lead to optical gain. For a given carrier density in the valence or conduction band, $N_{C,V}$, the quasi-Fermi level can be calculated by inverting the equation,

$$N_{C,V} = \int_{E_{C,V}}^{\pm\infty} g_{C,V}(E) f(E) dE, \tag{2.7}$$

where f(E) is given by eq. 2.6, $E_{C,V}$ is the energy of the bottom/top of of the conduction/valence band, and $g_{C,E}(E)$ is the density density of states in the conduction or valence band. This is essentially a statement of particle conservation.

The statistics of phonon excitations behave differently than electrons, as they are bosons rather than fermions. Here, the Bose-Einstein distribution deterimines the occupancy of each mode,

$$f(E) = \frac{1}{e^{\frac{E}{k_b T}} - 1}. \tag{2.8}$$

This differs from eq. 2.6 by the sign in the denominator, as well as the lack of a chemical potential. This reflects the fact that phonon number is not conserved and a phonon can be added with no cost of energy analogous to the statistics of photons. However, some work suggests that in non-equilibrium situations, photons can have a non-zero chemical potential, and it is possible that the same principle holds for phonons(24).

In our experiments, equilibrium occupancy of optical modes is relatively low, as the optical phonon energy is comparable to k_bT at room temperature. However, large non-equilibrium populations, or hot phonons, can be excited during electron relaxation. Using Raman scattering, where the relative heights of the absorption and emission peaks give an indication of occupancy, effective temperatures over 1000 K have been reported for optical phonons near the zone center(25).

2.1.5 Localized States

The electron and phonon dispersions discussed so far have been for semiconductors with a perfect lattice that is infinite in extent. In real semiconductors, impurites, interstitial atoms, vacancies, and bulk and surface defects all have electronic and vibronic states. If the density is low enough that no aggregates form, these imperfections result in localized electronic and vibrational modes. Here, a k-space description does not necessarily

apply in the same way, as a localized state does not share the same infinite periodicity as the lattice.

The nature of the electronic states of bulk imperfections is quite variable. In many cases, they can be thought of analogously to molecules or atoms embedded in the lattice with discrete vibrational and electronic levels. When these levels are close to the band edges they are considered traps, and they act as scattering centers for conduction band electrons. When they are near the middle of the gap they are called deep levels where non-radiative recombination can occur.

A configurational coordinate diagram is often used to describe these centers. The configurational coordinate diagram is analogous to reaction coordinates from chemistry, where many degrees of freedom are simplified to one abstract coordinate(26). A simple example of one of these diagrams is shown in fig. 2.4. There is an excited and ground electronic state, each with multiple vibrational levels. When the system can transition directly from the excited to ground state without a change of energy, or reaction coordinate, a non-radiative transition can occur.

After transitioning to the ground electronic state, the system can vibrationally relax by sequential emission of phonons to the surrounding lattice. In this diagram it is apparent that this transition can occur when the system is vibrationally excited, so that higher temperatures result in faster non-radiative rates. The relaxation rate of these types of centers is governed by Shockley-Reed-Hall recombination(27). This type of recombination is dominant in indirect-gap semiconductors such as silicon or germanium, where the carrier lifetime is on the order of microseconds at room temperature.

2.2 Dynamics

In our experiments, we are interested in using the tools developed so far to understand dynamical processes, such as transport and photoexcitation. In most cases, a semiclassical treatment where the Boltzmann transport equation,

$$\partial_t f + \mathbf{v}(\mathbf{k}) \cdot \nabla_{\mathbf{r}} f + \frac{\mathbf{F}_{ext}}{\hbar} \cdot \nabla_{\mathbf{k}} f = (\partial_t f)_{scat}, \tag{2.9}$$

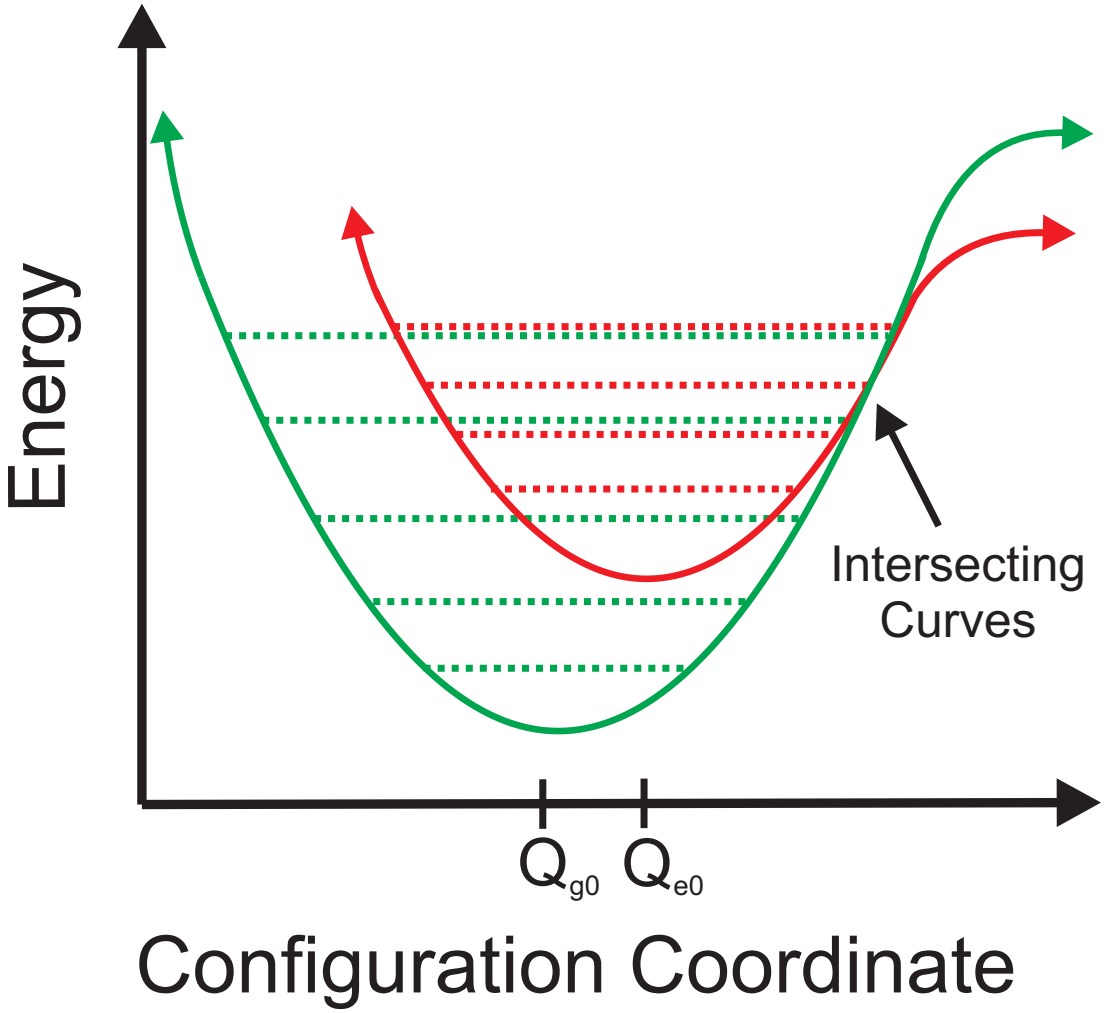

Figure 2.4: Configurational Coordinates - Energy levels of a non-radiative center, as a function of configuration coordinate Q. For the example of an impurity atom, Q would be the average distance of neighboring atoms. The dotted green (red) lines indicate the vibrational levels of the electronic ground (excited) states. In the vibrationally and electronically excited state, the system can transition directly to a highly vibrationally excited ground electronic ground state where the curves intersect (indicated on the diagram). Sequential release of phonons to the crystal lattice completes the process of non-radiative recombination.

is used to understand how the distribution, *f(**r**,**k**)*, of particles evolves in phase space as a function of time(28). Here, the terms on the left hand side describe the behaviour of a distribution of free particles with velocity $\mathbf{v}(\mathbf{k})$ in an external field, $\mathbf{F}_{ext}$. The scattering term, on the right hand side, arises from processes which interupt the free particle motion. Rather than deal with calculating the effect of each individual phonon or impurity, for example, they are instead treated statistically. Scattering events redistribute electrons among the states at a rate which can be determined from Fermi's golden rule. In this case the matrix element depends on the nature of the scattering mechanism.

In ultrafast experiments, we generate a new distribution within a narrow range of energies. We are then interested in how it evolves as a function of time thermalizing with itself and with the lattice before relaxing back to an unexcited state. In high-field transport, we study how carriers are redistributed within the excited state due to an external field. Here, we will outline some general features of the evolution of a distribution in such experiments.

2.2.1 Absorption of Light

The dipole matrix element is used to determine the rate of absorption, similarily to the rate of emission, and is typically a constant value near the band edge. The absorption coefficient scales proportionally to the joint density of states,

$$\alpha \propto \mu^{3/2}\sqrt{E_\gamma - E_g}, \tag{2.10}$$

where μ is the reduced effective mass of the conduction and valence bands, and E_γ is the photon energy. The absorption coefficient is zero for photon energies smaller than the gap, and for larger energies increases proportionally to the square root of the excess energy, $E_\gamma - E_g$. The effective masses in GaAs and InP are similar, and for the same excitation fluence and center frequency the absorption coefficient in InP is higher than that of GaAs as the bandgap of InP is smaller than GaAs.

Here we have assumed linear absorption. Following this assumption, we can make an estimate of the carrier density. The intensity of light, or number of photons, decays exponentially as a function of depth in a material. To simplify the calculation, we assume uniform carrier density in a cylinder of radius r (the excitation spot radius), and height $\delta = \alpha^{-1}$. For an incident pulse with energy W and center frequency f the carrier density is,

$$\rho = \frac{N}{V} = \frac{W}{hf}\frac{T\left(1-e^{-1}\right)}{\pi r^2 \delta}, \tag{2.11}$$

where T is the transmission coefficient, 1-e^{-1} is the fraction of carriers absorbed in within penetration depth, and, h is the usual Plancks constant. In terms of eq. 2.9, optical excitation can be thought of as injecting carriers with well-defined energy and position. The distribution of injected carriers, before scattering, is similar to a set of gaussian functions with one for each valence band from which carriers can be excited.

This calculation assumes linear absorption, which breaks down on short timescales and high excitation densities. Spectral hole burning decreases the absorption coeffiecient in the case where the excited state occupancy fills more rapidly than it is depleted by scattering processes(29). At extremely high densities, all of the excited states become occupied, and the absorption edge moves to higher energies, analogous to the Burstein-Moss shift where there is a blueshift of the absorption edge due to doping(30). At the excitation densities used in this study, nonlinear absorption is likely to occur. As a result, trends in data will be discussed in terms of pump power, only providing an estimate of carrier density.

2.2.2 Coulomb Scattering

For carrier-carrier scattering, the perturbation hamiltonian is the couloumb interaction between charged particles. The scattering rate is strongly density dependent, with time constants ranging from tens of picoseconds to tens of femtoseconds for carrier densities of 10^{15} and 10^{18} respectively cm^{-3}. Electron-electron, electron-hole, and hole-hole scattering all occur at slightly different rates, proceeding most rapidly for particles with

similar effective masses.

In our experiments with high excitation density, carrier-carrier scattering efficiently thermalizes electrons and holes on timescales shorter than the duration of the excitation pulse. The electron and hole distributions can be described by eq. 2.6 almost instantaneously. As a result, the PL spectrum contains no remnant structure of the excitation pulse. This is not the case for low excitation density and low temperature(31).

Coulomb scattering is an elastic process, and the carrier system does not dissipate energy in this phase of relaxation. As the timescale for carrier scattering is much more rapid than phonon scattering, a hot electron distribution with effective an temperature much higher than ambient is formed.

In one sense, carrier-carrier scattering does not play an important role during transport. It can be ignored in the simulation of equilibrium transport using the Boltzmann equation. However, in another sense, the collective response of electrons, a plasmon, governs the AC conductivity. For a free electron gas the dielectric constant is given by,

$$\epsilon_r(\omega) = 1 - \left(\frac{Ne^2}{\epsilon_0 m*}\right)\frac{1}{\omega^2 + i\omega/\tau}, \tag{2.12}$$

where, ϵ_r is the relative dielectric constant, e is the elementary charge, ϵ_0 is the permittivity of free space, ω is the frequency of the electric field, and τ is the scattering rate(32). The quantity in brackets is the square of the plasma frequency, ω_p,

$$\omega_p = \left(\frac{Ne^2}{\epsilon_0 m^*}\right)^{1/2}, \tag{2.13}$$

The Coulomb interaction between electrons and holes is also responsible for the formation of bound states (excitons) with energy in the forbidden gap(33). Generally, the contribution of excitons to optical properties can be neglected when the binding energy is much lower than the ambient temperature. This is the case in our experiments. However, Kaindl *et al.* have observed strongly enhanced excitonic behaviour in quantum wells, even with ambient temperature several times that of the binding energy(10).

2.2.3 Carrier-Phonon Scattering

Electrons can also scatter off of lattice vibrations, where the perturbation hamiltonian can take several forms. The local variation in lattice constant of longitudinal oscillations results in a change in bandgap. This is known as deformation potential scattering, and the resulting matrix element is independent of wavevector. In zincblende semiconductors, the dipole moment of the phonon results in polar optical electron-phonon coupling, governed by a Frölich Hamiltonian(34). Here the coupling strength near k=0 is strong, but drops off as the inverse square of the wavevector.

While electrons can absorb a phonon anywhere in the lattice, there is a threshold for phonon emission given by the zone center phonon energy. The zone center acoustic phonon energy is zero, so that acoustic phonon emission is always possible. Conduction band electrons at the bottom of the Γ-valley can only scatter off of low wavevector phonons.

As the energy increases, larger wavevector transfer is possible, and there is a higher density of final states. The result is an increasing scattering rate with carrier energy. Carriers within one LO phonon energy of the X or L minima can undergo intervalley scattering, which occurs via deformation potential interaction with zone edge phonons. These principles are summarized in fig. 2.5.

After ultrafast excitation, electron-phonon coupling is responsible for bringing the lattice and carrier system to thermal equilibrium over several picoseconds. The scattering rate for acoustic and optical phonons are similar(35), however the cooling process is dominated by optical phonons, as more energy is exchanged with each scattering event. At high excitation densities, the cooling process can be slowed due to the presence of hot phonons, as the statistical weight of phonon absorption is increased relative to that of emission(36).

Intervalley scattering (3 and 4 in fig. 2.5) is also important in both optical excitation and high-field transport. If photoexcited electrons are injected with high enough energy to undergo intervalley scattering, the majority of carriers will first scatter to

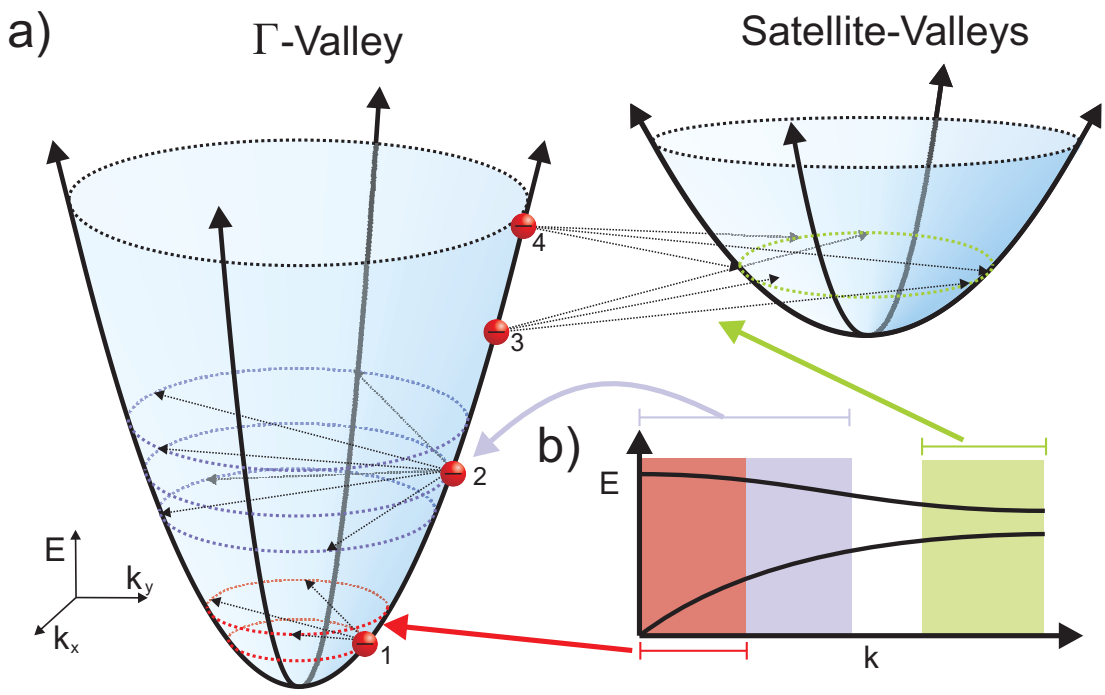

Figure 2.5: Electron Phonon Scattering - a) 2-D illustration of allowed scattering processes for various electron (red circles) energies. b) Schematic of the phonon dispersion curves, indicating which phonons contribute to electron-phonon scattering for electrons at position 1) below the threshold for phonon emission can only scatter by emission of zone center (shaded red in b) phonons. For acoustic phonons, the emission threshold is zero, while for optical phonons it is equal to the zone center phonon energy. 2) With with higher energy can both emit, and absorb phonons. The larger number of final states for the electron can scatter to, combined with the increased number of phonons which satisfy momentum conservation (shaded red and purple), increases the total scattering rate. 3 and 4) Electrons above the threshold for intervalley scattering by absorption (3) and emission (4) of a zone edge phonon (shaded green). Electrons at this energy can also scatter into the direct valley, similarily to 1 and 2 (not illustrated).

satellite valleys before relaxing to the bottom of the Γ-valley. This leads to a slow PL rise time and broadened spectrum, as the Γ-valley density is low and carrier temperature high while electrons scatter back from satellite valleys.

For high field transport in polar semiconductors, the drift velocity first overshoots the equilibrium value before the majority of carriers scatter to satellite valleys, where the effective mass is higher. The figure of merit for determining the fields required for velocity overshoot is the Gunn field, which is on the order of 10 kV/cm(37). The peak THz fields in free space used in this work are on the order of 200 kV/cm, which is much higher than the Gunn field. However, the transmitted field could be smaller than this, and the Gunn field could be relevant.

Intense THz fields drive intervalley scattering on sub-cycle timescales, modulating the optical conductivity by increasing the effective mass and scattering rate in eq. 2.12. This leads to self amplitude modulation and rectification of the incident pulse(13). This rectification leads to a spatial separation of the electron and hole distributions.

2.2.4 Surface Effects

A high density of localized states exists at surfaces or interfaces. At room temperature in equilibrium, electrons and holes diffuse towards the surface. As the effective mass of electrons is lower than holes, more electrons end up trapped in the surface, resulting in a built-in voltage and band bending. On excitation, a transient current surge occurs, spatially separating electrons and holes.

Additionally, both electrons and holes diffuse into the substrate, because of the gradient density. Electrons diffuse more rapidly into the substrate than holes, due to mass asymmetry, which is another source of transient current normal to the surface. This process, known as the photodember effect, results in spatial separation of electrons and holes(38). These current surges can be studied by collecting the emitted THz radiation(39).

After any transient dynamics have died down, there is a net drift of electrons into the substrate, once again due to the charge gradient, as well as towards the surface. With an untreated surface with high surface state density, drift towards the surface is limited by the drift velocity. This diffusion is associated with recombination as all carriers which reach the surface recombine non-radiatively. It is parameterized by the surface recombination velocity(40).

2.3 Summary

We will conclude with a brief summary of ultrafast excitation, shown in fig. 2.6. When an ultrafast pulse is incident on a semiconductor, a distribution of carriers with a narrow range of energies is generated, however, in our experiments Couloumb scattering thermalizes the distribution on timescales compared to the excitation pulse. For excitation near the gap, only a small number of carriers scatter to the satellite valleys, as in 2.6 a).

Over the next several picoseconds, there are both hot electron and hot phonon distributions as in 2.6 b). In this situation, carriers are more likely to absorb phonons than in equilibrium situations, and the cooling is slowed. PL in this regime is has a very broad spectrum which is considered hot luminescence. While the hot phonons are decaying, the electrons are also relaxing down to the bottom of the band. Any carriers scattered to the satellite valleys act as a resevoir of hot carriers as indicated by the carrier returning to the direct valley in 2.6 c). This Keeps the distribution hotter similarily to the hot-phonon effect. When excited in the presence of the intense THz pulse electric field many more carriers will scatter to the satellite valleys. As well as acting as a hot-carrier resevoir, this will slow the rise time of the luminescence by reducing the density in the Γ-valley.

After the carrier and phonon systems have thermalized, the remaining excited carriers must still recombine. In this regime, the full-width half-max (FWHM) of the luminescence spectrum is approximately $k_B T$. In this final stage we have also included a channel for non-radiative recombination. In principle it should be included in all figures as it is a probablistic process. Generally the timescales are much longer than

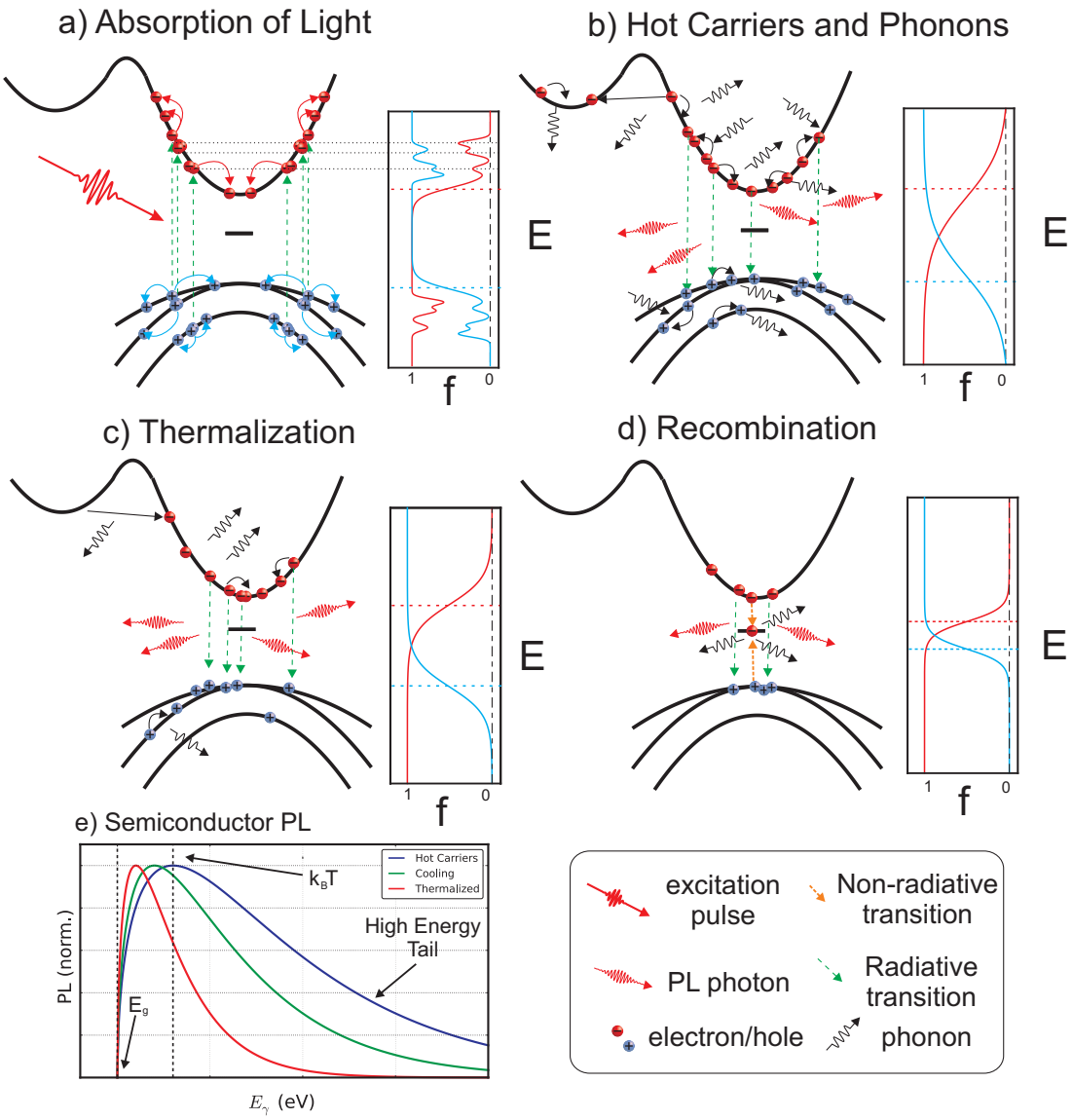

Figure 2.6: Illustration of Ultrafast Excitation - a) Absorption of an ultrafast pulse creates a carrier distribution with a set of peaks (inset), while Couloumb scattering quickly thermalizes the distribution. b) The first several picoseconds after excitation, where there are hot carrier and hot phonon distributions. The electron (red) and hole (blue) distributions with are shown to the right, where the dotted lines indicate the quasi-Fermi levels. c) The electron and phonon system cools over time, such that the number of phonons decreases and the electrons relax ot the bottom of the conduction band. Electrons which have scattered to satellite valleys can return, which heats the distribution. d) A photoexcited distribution which has cooled to the lattice temperature. e) Semiconductor PL spectra for different times, where hot carriers corresponds roughly to b), cooling to c), and thermalized to d).

the other listed processes so that this channel of recombination was only included in the final diagram.

The PL spectrum from each of these regimes is shown in fig. 2.6 e), it was calculated using eqs. 2.1 and 2.5. The broadest spectrum is associated with the earliest timescales, and the narrow with the longest. The lineshape is asymmetric, reflecting the nature of the density of states which increases with energy. Real semiconductor luminescence does not precisely follow this curve and there are always photons emitted with sub-band-gap energy.

Some studies associate the sub-gap luminescence emission from band tail states, e.g., the Urbach tail(41). By assuming a functional form for the tail states and convoluting these with the regular semiconductor states it is possible to fit the full PL spectrum(42). Alternatively, the mid-gap PL can be treated as a many-body effect, where optical emission occurs with the simultaneous emission of a plasmon broadening the emission linewidth(43). Interpreting both the emission as either broadened transitions or from mid-gap states reproduces experimental data well.

3

Experimental Details

In the previous chapter, we introduced the physics of semiconductors, and talked about ultrafast excitation and high-field transport. The tools we use to probe these materials are amplified femtosecond pulses from a Ti:Sapphire laser system (Coherent Micra/Legend) and intense THz pulses generated in LN by tilted-pulse-front optical rectification (OR). The laser amplifier operates at 1 kHz and outputs 3.5 mJ, 800 nm, pulses with 50 fs duration. The THz source is homebuilt, and characterized using a combination of wavefrom, pulse energy, and spot profiling, using EO sampling, a pyroelectric detector, and thermal imager respectively. Typical pulse energies of 2.0 μJ, and e^{-2} spot diameters of 1.8 mm result in peak electric fields of up to 230 kV/cm as measured by EO sampling.

The THz pulse is collected and focused onto GaAs or InP wafers using off-axis parabolic mirrors. The wafers are simultaneously photoexcited collinearly using near infrared (NIR) pulses split off from the same Ti:Sapphire amplifier. PL is collected non-collinearly and focused into an optical fiber, then measured using either 1) a photodiode to study integrated change, or 2) a monochromator and CCD (charge-coupled device) array for parallel detection or a slit and avalanche photodiode (APD) for single channel detection of the differential spectrum. Fig. 3.1 is a schematic of the experimental setup. In the following sections, each component will be described in more detail.

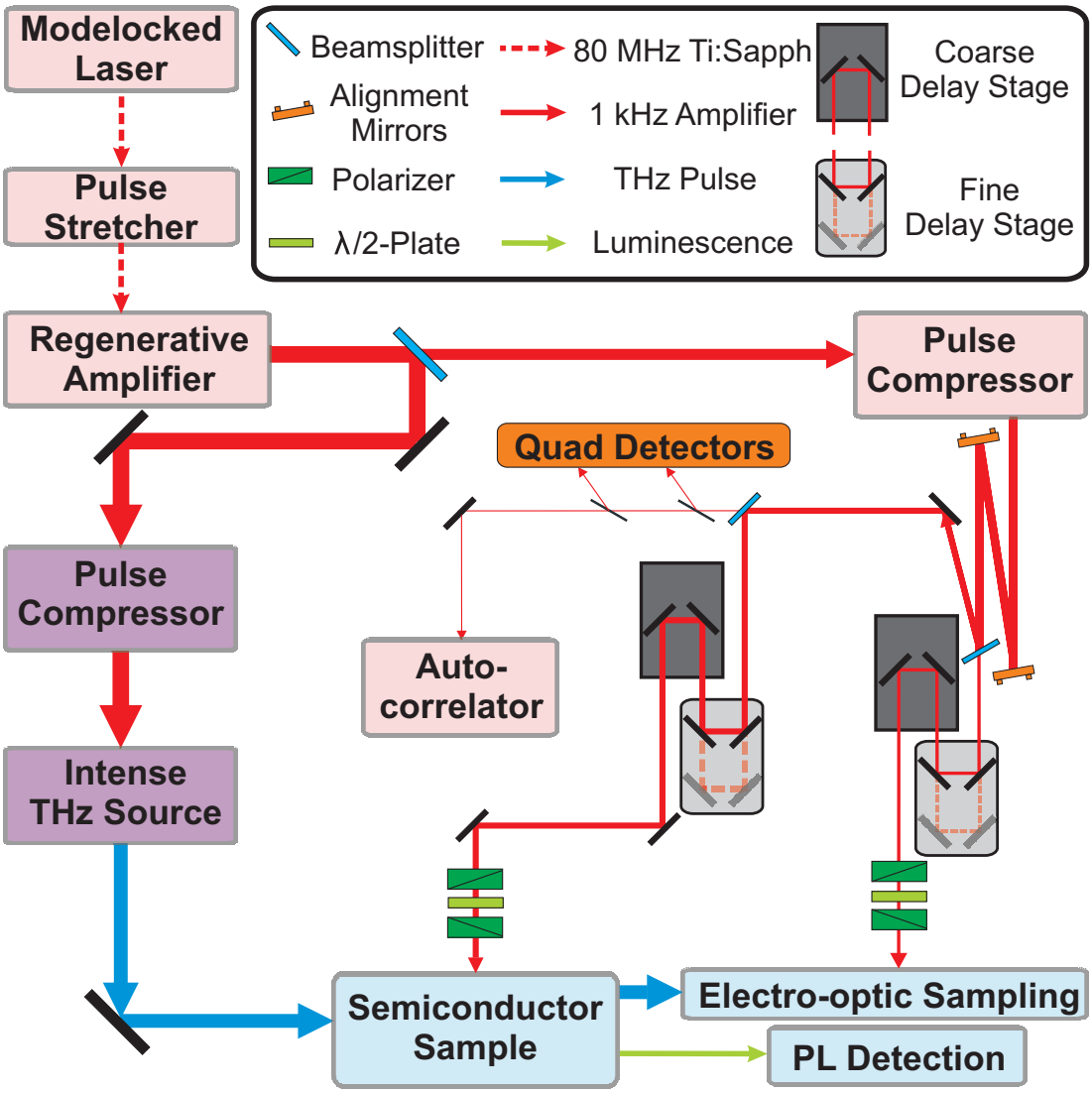

Figure 3.1: Schematic of Experiment Setup - A Ti:Sapphire laser oscillator (Coherent Micra) seeds a 1 kHz regenerative amplifier (Coherent Legend). The output of the amplifier is split into several beams used for THz generation by optical rectification of tilted pulse fronts in lithium niobate, photoexcitation of luminescent semicondutors, and electro-optical sampling. The components are roughly color coded as Coherent Inc. products (pink), THz source components (purple), THz modulation of PL (blue), and alignment tools (orange).

3.1 Laser System

3.1.1 Oscillator

The laser oscillator (Coherent Micra) is a mode-locked, 80 MHz repetition rate Ti:Sapphire lasers pumped by the second harmonic of a continuous wave (CW) Nd:YVO_4 diode pumped laser (Coherent Verdi V5), which outputs 5 W at 532 nm. It is passively mode-locked, based on the principle of kerr-lensing, where the self focusing of an intense pulse leads to better overlap with the pump in the gain medium. The cavity therefore favors mode-locked vs. CW operation(44). A pulse compressor consisting of a prism pair is inserted into the cavity, as seen in fig. 3.2 a). Once mode-locked, pulse propagation in the cavity behaves as a soliton resulting in a stable regime where the positive group velocity dispersion (GVD) of the Ti:Sapphire crystal is balanced by the negative GVD of the prism compressor(45).

The pulse characteristics can be tuned by translating the prisms in and out of the beam to adjust the group delay. An adjustable slit can also be used to physically block portions of the spectrum. In fig. 3.2 b)-d), the laser spectrum is shown tuned to 40 nm, 50 nm, and 80 nm bandwidth respectively. More insertion results in more bandwidth, however with too much negative GVD the soliton mode-locking regime is lost, and other mode-locking mechanism can dominate(46, 47). Another common problem is shown in 3.2 d), the sharp peak in the spectrum is due to CW breakthrough. It is important to avoid this when tuning. We typically operate the laser in the 40 nm bandwidth condition for 2 reasons: 1) as bandwidth increases, the secondary peak (seen at 750 nm in fig. 3.2 c) increases in amplitude, and 2) it results in more stable long term operation.

3.1.2 Amplifier

The pulse train of the oscillator is routed to a stretcher, and used to seed a chirped pulse regenerative amplifier (Coherent Legend). The pulse is first stretched to several hundred picoseconds, to prevent damage of the crystal during amplification(48). Pulses are injected into a secondary laser cavity at 1 kHz repetition rate using a pockels cell, where they make approximately 15-18 round trips before being ejected by a second pockels cell in combination with a brewster window. The crystal in this cavity

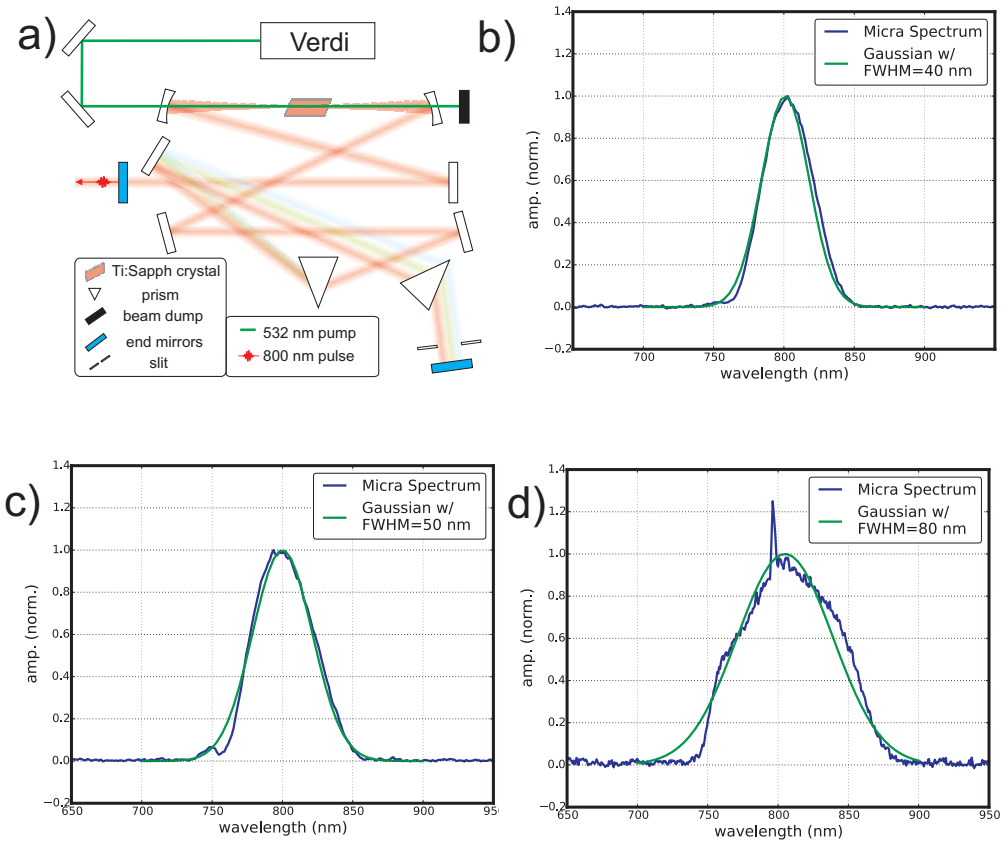

Figure 3.2: Laser Oscillator - a) Schematic layout of the mode-locked laser system. b)-d) Laser spectrum tuned for various conditions. A combination of translations from both prisms was used to obtain these spectra. Inserting more of the prism into the beam typically results in more bandwidth, however too much makes the laser makes the system unstable. The spectrum is adjusted by translating the prisms in the cavity, which compensate for dispersion in the Ti:Sapphire crystal. In c), a small peak in the spectrum can be seen at 750 nm. The origin of this behaviour is not known, and great care must be taken during alignment to minimize this peak and obtain a Gaussian spectrum. In d), the peak in the spectrum is due to CW breakthrough. The amplifier should not be run with this feature present in the spectrum.

is pumped by a 30 W Q-Switched 532 nm laser (Coherent Evolution). The 800 nm pulses are recompressed after ejection from the regenerative amplifier.

The bandwidth of the output of the amplifier is in general less than that of the oscillator, with a nearly Gaussian profile centered near 800 nm, with a FWHM of 26 nm. Although the exact pulse characteristics change with alignment, an example of the spectrum is shown in fig. 3.3 a). Fig. 3.3 b) shows the effects of the high power beam propagating through a glan-laser polarizer (Thorlabs) without attenuation but with a modified spectrum. If the laser power is attenuated before the polarizer, the spectrum remains unmodified. This nonlinear behaviour is characteristic of SPM (self-phase modulation), and should be avoided as it introduces undesireable pulse qualities.

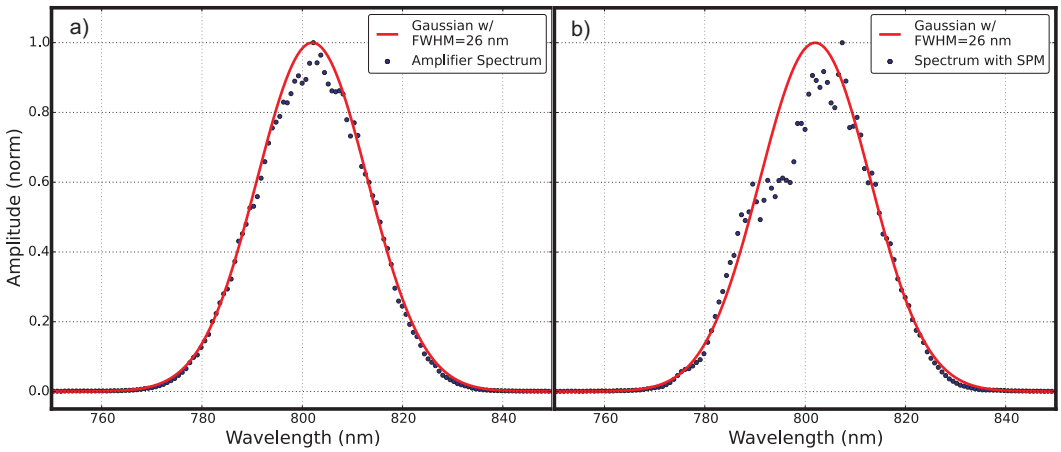

Figure 3.3: Amplifier Spectrum - a) Laser spectrum after amplification, showing a nearly Gaussian profile with bandwidth of 26 nm, lower than that of the oscillator. b) Laser spectrum after a glan laser polarizer without attenuation, displaying a modified spectrum. For the results presented in this thesis, a neutral density filter is used before the polarizer to prevent this effect.

The temporal behaviour of the pulse is measured using an autocorrelator, as shown in fig. 3.4 a). Here, the laser pulse is passed through a beamsplitter, and the pulses are mixed in a beta barium borate (BBO) crystal crossing at a small angle. The intensity of the second harmonic, I_{SHG}, is measured as a function of delay, τ,.

$$I_{SHG}(\tau) = \int_{-\infty}^{\infty} I_{FF}(t) I_{FF}(t-\tau) dt, \tag{3.1}$$

where I_{FF} is the intensity of the incident pulse. We use a single-shot configuration where the delay is projected spatially onto a linear CCD array, and measured using an oscilloscope. A calibration is obtained by delaying one of the beam paths by a known amount and measuring the shift of the peak of the trace. For the system used in our experiments (Coherent Inc.), translating the stage by 0.1 mm shifts the peak of the trace by 1.43 ms, giving a calibration factor of 0.47 ps/ms.

The trace in fig. 3.4 a) is calibrated and fit to a Gaussian function with a FWHM of 79 fs. Assuming the laser pulse has a Gaussian temporal profile, the autocorrelation trace is longer than the pulse duration by a factor of $\sqrt{2}$. The pulse duration would then be 56 fs(49). However, the wings on the autocorrelation trace are an indication of a pulse with cubic phase, and therefore not Gaussian.

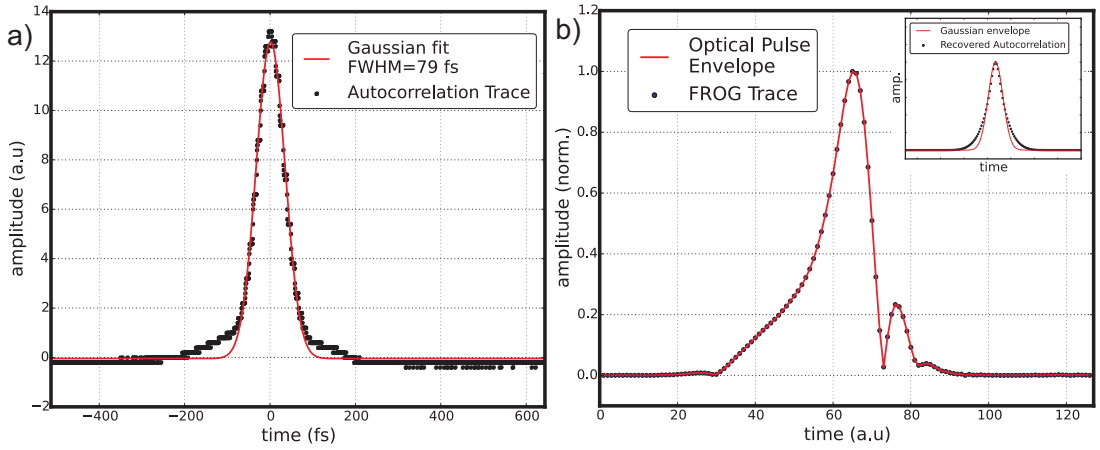

Figure 3.4: Temporal Characterization of the Amplified Pulses - a) Intensity autocorrelation, measured with a single shot autocorrelator. A FWHM of 79 fs translates to a pulse duration of 56 fs, assuming a Gaussian envelope. However, the wings of the trace, where a Gaussian function does not fit the data, are an indication of cubic phase and a non-Gaussian envelope. b) An uncalibrated FROG trace, which shows the electric field envelope. The multiple peak, asymmetric structure is characteristic of cubic phase. Inset: Autocorrelation reconstructed from the retrieved FROG trace, showing similar non-Gaussian structure to a).

Proper characterization of cubic phase requires more sophisticated techniques, such as Frequency Resolved Optical Gating (FROG)(50). This method is similar to an autocorrelation, except that the second harmonic spectrum is measured as a function

of time delay, and the signal is given by,

$$I_{FROG}(\omega,\tau) = \left| \int_{-\infty}^{\infty} E(t)E(t-\tau)e^{i\omega t}dt \right|^2 \tag{3.2}$$

Using a phase retrieval algorithm, the electric field envelope can be recovered from the FROG trace(51). In chapter 4, results will be presented where the THz modulation of PL is strongly affected by the compressor setting. Some indications have shown asymmetry with respect to chirp direction. In order to understand the origin of these effects, we are currently developing an implementation of frequency-resolved optical gating(52). A recovered trace is shown in fig. 3.4 b).

These results are prelimanary and the time axis is uncalibrated, however, this figure is included to give a possible interpretation of the asymmetry in some of our results. The multi peak structure of the envelope is a characteristic of cubic dispersion which is a common feature of amplified pulses. The inset shows the solution to eq. 3.1 with the reconstructed FROG trace as the input, i.e, the autocorrelation of the FROG trace. The wings on the trace are qualitatively similar to the experimentally acquired autocorrelation in 3.4 a).

3.1.3 Beam Routing

After ejection from the cavity, the pulse is immediately passed through an 80-20 beam splitter. Separate compressors are used for each beam, with the 80% going to a home built grating compressor, and the 20% beam going to the Legend amplifier internal compressor. In this way, the pulse duration for the THz generation beam can be controlled separately from the other beams. The 20% power beam is further split into high, medium, and low power beams used for photoexcitation, electro-optic sampling, and diagnostics respectively.

The high and medium power beams pass through both rough (92 cm travel) and fine (15 cm travel) computer-controlled delay stages. This results in a full scan window of 107 cm, or 7.1 ns. For a given experiment, the rough stage is typically fixed in a convenient location which puts t_0, the point where any two beams arrive at the same

time, near the middle of the fine delay stage.

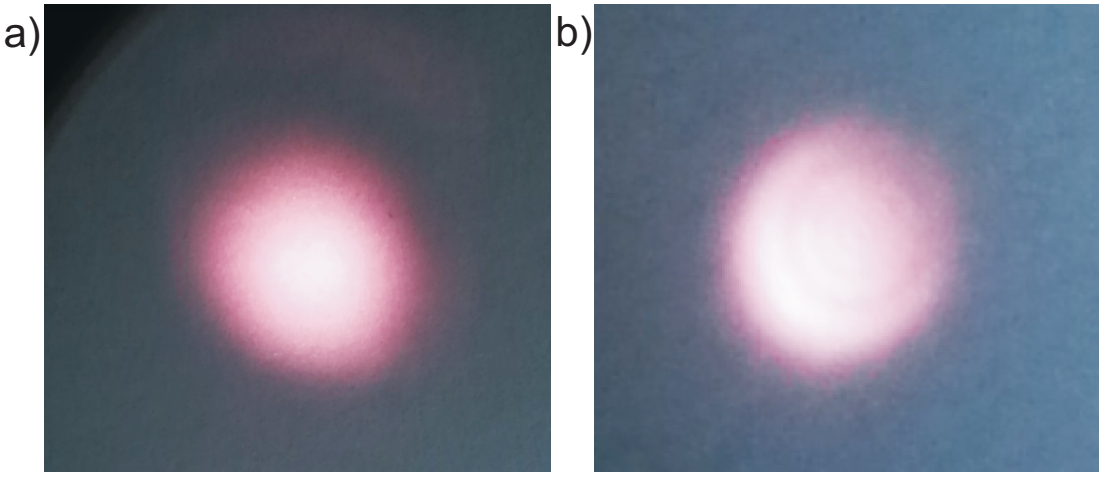

Figure 3.5: Effect of clipping - Image of the laser spot on a white screen taken with a phone camera. In a) the laser propagates through a wide open aperture. Careful examination reveals a very dim strip above the main spot of the laser. This feature is more easily visible to the naked eye, and is present after amplification. In b), the aperture is partially closed, and the screen is placed approximately 50 cm away, showing interference fringes. The fringes, and other features, generally become more prominent, and other features develop with increasing propagation distance.

Care must be taken to preserve laser pulse quality during propagation along the bench. Clipping results in interference fringes in the mode of the laser, as seen in fig. 3.5. The beam size at the delay stages is almost as large as the apertures, and proper beam pointing at these points is critical. To facilitate this alignment, a small amount of the low power (diagnostics) beam is split off and sent to a quad detector in two locations. The first two mirrors after the compressor are used to balance the quads on a daily basis.

3.2 Intense THz Source

The 80% beam from the amplifier is used for intense THz generation using tilted pulse front pumping (TPFP) OR in LN(12). Here we will not present an in depth theoretical description of THz generation by OR, which can be found in many papers, for example refs.(53, 54, 55, 56). Instead, we simply give the reader a short, intuitive description

of the technique. In OR, an ultrafast pulse propagating in an EO crystal produces a transient polarization at THz frequencies by beating between the various frequency components (difference frequency generation in the Fourier domain).

In index-matched crystals, the polarization radiates a field and the amplitude grows linearly with propagation distance. Here, constructive interference during propagation occurs across the full pulse front, and a spatially-extended high power pulse can be used, as seen in fig. 3.6 a). In index mismatched crystals, a point optical source can be used and constructive interference results in a Cherenkov cone of radiation. A spatially-extended pulse cannot be used in the same way due to the lack of constructive interference along the pulse front(57). Instead, an extended source can be used by tilting the intensity front along the Cherenkov cone angle θ, as seen in fig. 3.6 b).

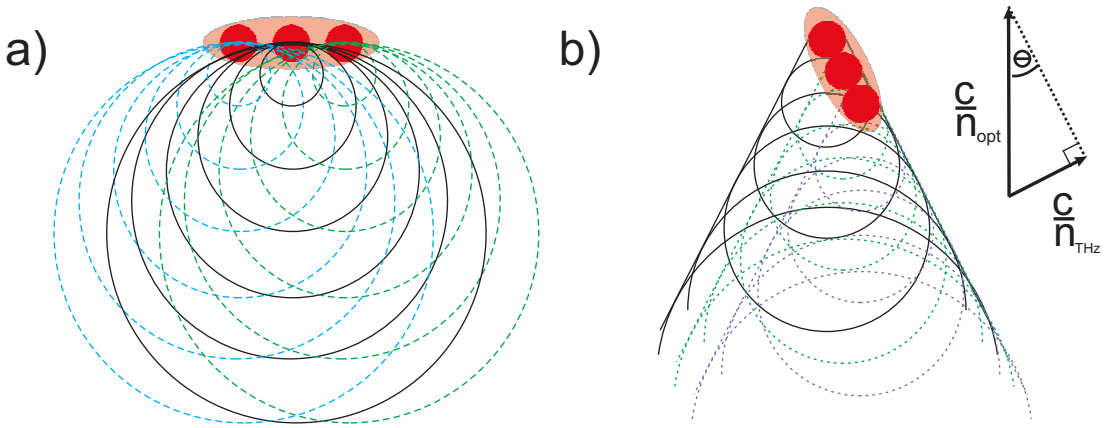

Figure 3.6: Optical Rectification - In THz generation, the emitted radiation is dependent on phase matching. a) Dipole radiation generated at different times (signified by the increasing size of the black circles) in a phase matched crystal propagates at the same velocity as the generation pulse and constructive interference occurs collinearly. The source can be extended spatially and constructive interference still occurs (signified by the blue and green dotted curves). b) Dipole radiation in a phase mismatched crystal such as LN creates a Cherenkov cone. THz generated from a spatially extended source interferes constructively if the intensity front of the pump pulse is tilted along the angle θ (top right).

After the generation crystal, THz pulses are collected and focused with off-axis parabolic mirrors. Pulse characterization is done using a combination of a pyroelectric detector for pulse energy (Spectrum Detector), a thermal imager consisting of an array of pyroelectric elements (Electrophysics), or electro-optic sampling in a gallium

phosphide (GaP) crystal. The arrangement is shown in fig. 3.7.

3.2.1 Pulse Front Tilting Optics

The beam is first reduced by a factor of 2 using a Keplerian telescope arrangement with 200 and -100 mm focal length lenses. Several demagnification factors were tested, and this lens combination was chosen as it resulted in the highest conversion efficiency based on energy measured by a pyroelectric detector. A diffraction grating with groove density N=1800 $ln\ mm^{-1}$ angularly disperses the beam to induce pulse front tilt, and a 4f plano-convex sperical lens system images the pulse into the crystal.

The 4f imaging configuration was chosen to reduce spatio-temporal distortion, where the imaging of an angularly dispersing pulse introduces temporal spreading proportional to the distance from the axis of the lenses(58). It should be noted that some groups use cylindrical (59) instead of spherical lenses to remove temporal aberrations in the vertical dimension. As the pulse is not angularly dispersing in the vertical dimension, the temporal smearing should be small(60). A direct comparison between cylindrical and spherical lenses has not yet been published.

The focal lengths of the lenses are 125 mm and 75 mm, resulting in a demagnification factor D=1.67. This demagnification-grating combination satisfies the conditions specified in ref. (55). The design criteria is meant to minimize the pump pulse duration along the intensity front, avoiding imaging distortion. Finally, based on the demagnification, D, and groove density per unit length, N, we can calculate the diffraction angle β which results in required pulse front tilt ($\gamma = 63°$),

$$tan(\gamma) = -\frac{N\lambda_{op}D}{n_{_{LN}}cos(\beta)}, \tag{3.3}$$

where, n_{LN} is the index of LN at the pump wavelength, λ_{op}=800 nm, and β is the diffraction angle given by,

$$N\lambda_{op} = sin(\alpha) + sin(\beta) \tag{3.4}$$

where α is the angle of incidence. The required angle of incidence is therefore 36.8°, resulting in a diffraction angle of 57.2°. These parameters are summarized in fig. 3.7. A

full derivation of these equations can be found in ref. (61). The efficiency of the grating is maximum when the magnetic field is polarized along the grating grooves (horizontal polarization in our case), while the c-axis (nonlinear axis) of the LN crystal is oriented vertically, thus a half wave plate is inserted between the final lens and the crystal.

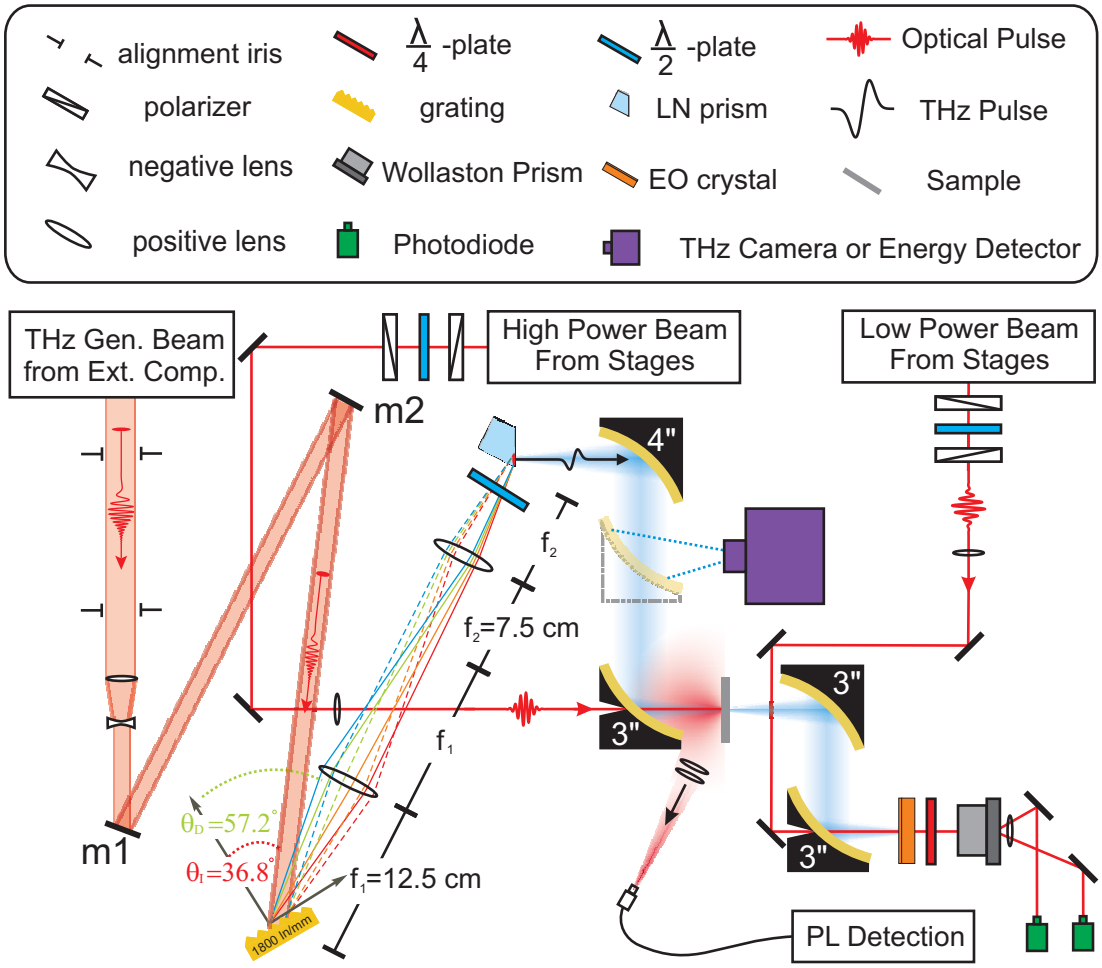

Figure 3.7: THz Source Layout - Schematic layout of the intense THz pulse source used in this study. A diffraction grating with 1800 *ln/mm* is used to introduce angular dispersion into the laser pulse, which is imaged into a lithium niobate prism using a 4f imaging scheme. THz radiation is generated non-collinearly.

3.2.2 THz Routing Optics

Gold coated, 90° off-axis parabolic mirrors are used to collect and focus the emitted THz radiation, as shown in fig. 3.7. The mirror arrangement was modelled after that of ref. (62) where 4" and 3" focal length mirrors collect and focus the THz radiation respectively. The 4" parabolic was chosen such that diffraction of a Gaussian pulse with a beam waist of $w_0 = 1\ mm$ at the source, and 0.5 THz center frequency ($\lambda = 0.3\ mm$) would have a beam waist, w, large enough to fill the 2" aperture of the mirror at distance x=4" from the focus, calculated using,

$$w^2(x) = w_0^2 \left[1 + \left(\frac{\lambda x}{\pi w_0^2}\right)\right]. \tag{3.5}$$

The 3" focal length of the focusing mirror is chosen to achieve a smaller beam waist at sample position. Additionally in our set up, a mirror can be inserted in the collimated section before the focus optic in order to measure the energy or profile of the THz pulse. Two 3" focal length mirrors are placed after the sample position to route the beam to a secondary focus for EO sampling. Many groups use an alternative arrangement where a beam expanding mirror placed immediately after the source crystal to achieve spot sizes approaching the diffraction limit, as in ref. (59).

3.2.3 Electro-Optic Sampling Setup

In this study a 200 μm thick [110] GaP active layer, optically bonded to a 2 mm thick [100] GaP wafer, was used for EO sampling. The active layer of the EO crystal is placed at the focus of the final parabolic mirror with the field oriented in the $[1\bar{1}0]$ direction. The pockel's effect from the THz electric field induces a birefringence in the crystal at optical frequencies that is sampled by an initially linearly polarized co-propagating probe pulse. In velocity matched crystals, over distances less than the walk off length, the differential phase retardation $\Delta\phi$ is linearly proportional to the instantaneous electric field of the THz pulses according to,

$$\Delta\phi = \frac{\omega L}{c} n_0^3 r_{41} E_{THz}, \tag{3.6}$$

enabling measurement of both the amplitude and phase of the waveform(63). Here, c is the speed of light, L is the length, and r_{41} is the electro-optic coefficient of the

crystal. A quarter waveplate is introduced after the crystal, and a Wollaston prism is used to separate the horizontally and vertically polarized components angularly and the intensities of each (equal in the case of no THz) are measured by Si photodiodes (Thorlabs PDA100A). As the delay between optical and THz pulses is changed, the electric field of the THz pulse is projected onto the balanced diodes according to,

$$I_{x,y} \approx \frac{I_0}{2} \left(1 \pm \Delta\phi\right), \tag{3.7}$$

where I_0 is the intensity of light incident on the EO crystal. The medium power beam from the Legend is used as the probe beam and is coupled to the beam path of the THz pulse collinearly through a small hole in the final parabolic mirror. Originally, a pellicle beam splitter (transparent to THz, partially reflecting to optical) was used. However alignment with this method was more difficult. Coupling the beam through the hole in the parabolic mirror ensures co-propagation which is more difficult to achieve with a pellicle.

On a final note, care must be taken to minimize the duration of the probe pulse in order to accurately calibrate the electric field and prevent red-shifting of the spectrum. This can be done immediately before the EO setup using a BBO crystal by maximizing the intensity of second harmonic generation (SHG). When compared to an actual measurement in an autocorrelator, this method is accurate within 10 fs.

3.2.4 Source Alignment

There are a large number of degrees of freedom in alignment of tilted-pulse-front THz sources and they require frequent maintenance. The purpose of this subsection is to develop an informal guide to troubleshooting any problems which may arise during operation. We will operate on the assumption that the beam pointing is aligned to the irises along the input path and that the laser is operating correctly.

The simplest measurement to make is the energy reading, and it should be taken before any adjustments are made. Place the removable mirror against the stops, and insert the pyroelectric detector on a magnetic mount into it's base. The detector should

be attached to the computer by a USB cable, and the software interface (SXI-D Detector program) should be running. For maximum sensitivity set the range to 2 μJ. On this setting, the energy reading on the computer should fluctuate around 0.05 μJ, and it should spike when tapping the detector head gently (this should be visible on the oscilloscope as well).

A signal should be visible on the oscilloscope if there is a THz pulse present. If not, there are a number of common problems which are not related to the pointing of the laser, and before realignment check that:

- the green light on the back of the detector is on and it is communicating properly with the software
- the oscilloscope is triggered and the termination is set to 1 MΩ (AC or DC coupling both work)
- the oscilloscope window is set correctly
- the pyroelectric element is located at or near the focus of the parabolic mirror
- the wiregrid polarizers are not crossed, and the removable parabolic mirror is seated correctly against the beam stops.
- there is nothing obstructing the beam path of either the 800 nm pump beam, or the THz beam

It is useful to note that the LN crystal glowing brightly blue is correlated with efficient THz generation, and there should be a signal present. However, if there is no signal after each of these checks, there could be a problem with beam alignment. The first thing to check is that the beam is at 6" height along the path from M2 to the grating in fig. 3.7, and centered vertically on each lens in the 4f system. If these conditions are satisfied, and there is no signal from the pyroelectric, a full alignment could be required.

To begin, it is important to fix the position and angle of the LN crystal with respect to the focus of the collection parabolic. A removable iris can be inserted into the empty post holder below the crystal such that the aperture is located at the focus when the iris is closed. If a piece of paper is placed behind the iris and illuminated with a lamp,

a bright spot can be seen at each focus along the propagation direction.

The pyroelectric detector should be placed such that the aperture of the attached iris is right at the focus. The process can be repeated in the inverse propagation direction using a scattering sheet on the back of the pyroelectric iris. The LN prism should be placed such that exit face is parallel to the mirror and the focus is located approximately 1 mm from the entrance face. Throughout this process, it is important to verify that the location of the visible spot makes sense when compared to where the focus of the parabolic should be.

Once the LN position is set, the beam can be let through, making sure to carefully trace the beam path to be certain there is no danger from scattered light. Adjust the position of the beam on the crystal with the diffraction grating while monitoring the scope for a signal. If there is no signal, iteratively walk the beam along the diffraction grating with M2, and along M2 with M1 while keeping the beam pointed at the crystal with the diffraction grating. Throughout this process, check that the vertical position of the beam remains at a 6" height.

It is unlikely that the position of the mirrors or lenses needs to be adjusted to achieve a signal, and they should be left in place until a signal is obtained. Once a signal is obtained the lenses may need to be adjusted to optimize generation. If the desired pulse energy or electric field is not obtained by adjustment of the mirrors and grating alone, the rotation, distance from crystal, and, horizontal position in the beam path of each lens can be adjusted.

There are several other factors that affect the THz pulse. The second lens in the beam reduction section after the external compressor is on a stage, and its adjustment results in a change in energy. Typically, after adjustment the beam must be walked on the grating with M2 to achieve maximum energy. It is possible to achieve very high energies when the beam is diverging after this lens, however, this does not translate to the highest electric fields.

The pump pulse duration can be adjusted by moving the stage in the external grating, which can lead to increased generation efficiency. The position that results in maximum energy changes based on exact alignment of the laser. As well, the position of maximum compression is different depending how many round trips the pulse makes in the laser. Currently, the internal compressor is set at 18.8 mm for minimum pulse duration at the autocorrelator, and the external compressor is at 13.2 mm for maximum generation efficiency. Adjustment of the grating combined with z-translation of the second lens in the 4f setup can result in large gains in energy.

Optimizing the energy does not always result directly in the highest electric field, as measured by EO sampling. This could be due to divergence in the THz beam during the generation process, or a large THz beam waist, however, this is only speculation. In order to achieve the best correlation between a large energy measurement, and large electric field, the iris on the end of the pyroelectric detector can be closed, and the source can be optimized for maximum energy through the small spot. It is found that very different alignment is required to maximize energy with this condition.

3.2.5 Source Characterization

On a daily basis, the source operates with a pulse energy of between 2.0 and 2.3 μJ. The spot, as viewed with a thermal imager, is elliptical with dimensions of 1.7 mm (horizontal) by 2.4 mm (vertical), as seen in fig. 3.8 a). The exact dimensions vary with alignment. Although Gaussian at the focus, when viewed off the focus the mode is very distorted as shown in 3.8 c). A line scan scan of the off-focus pulse is shown in 3.8 d), where there is a main peak with potentially Gaussian character, and a second peak on the left side. This is consistent with some of the literature(64). There, the results were interpreted as being due to the optical pump pulse reshaping during generation due to cascaded nonlinear effects(53), and self-phase modulation (SPM)(54).

Figure 3.9 a) shows the THz waveform as measured by EO sampling. It is approximately single-cycle in nature, where the leading peak is almost 200 kV/cm, and the trailing peak is 230 kV/cm. The oscillations after the main pulse are due to a combination GVD in the generation and sampling crystals as well as absorption and

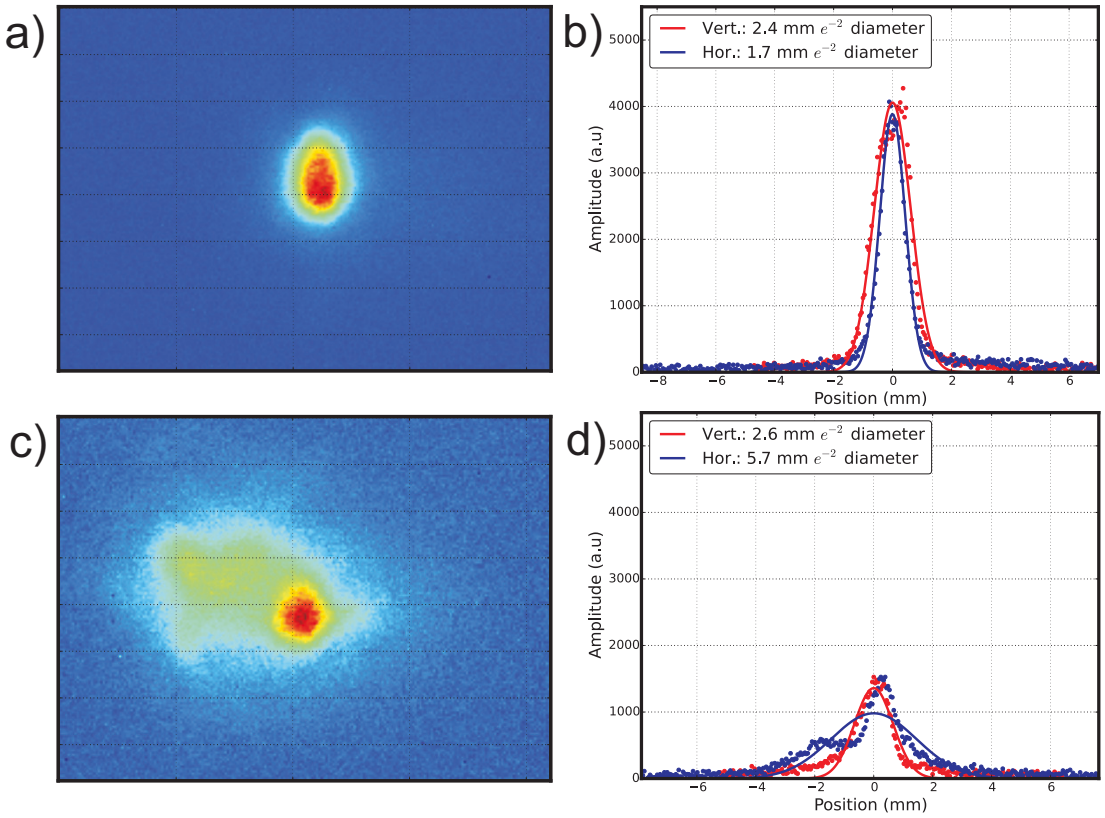

Figure 3.8: Spot Profile - a) THz spot measured using a thermal imager placed at the focus of the removable parabolic, with a slightly elliptical profile. b) Vertical and horizontal line scans. c) Horizontal and vertical profiles from the image in a), with a 2.4 mm vertical, and 1.7 mm horizontal e^{-2} diameter.

re-emission by water molecules due to periodic rephasing. If the system was put in a dry nitrogen environment, some of the oscillations could be removed.

The field calibration shown here is calculated using eq.3.6. There is another method for field calibration based on the spot area A, EO waveform w, and, pulse energy W3.8(65),

$$E_{THz} = \sqrt{\frac{\eta_0}{A \int w^2(t)dt}}, \tag{3.8}$$

where the area is calculated using the area of an ellipse, with axes given by the vertical and horizontal intensity beam waist, and, η_0 is the impedence of free space. Calcuation of the electric field with the two methods do not always agree, however, in the data presented here, using the measured pulse energy of 2.0 μJ, eq.3.8 results in a peak electric field of 225 kV/cm. This is very good agreement with the measurement from EO sampling. The two values sometimes differ by more than a factor of two.

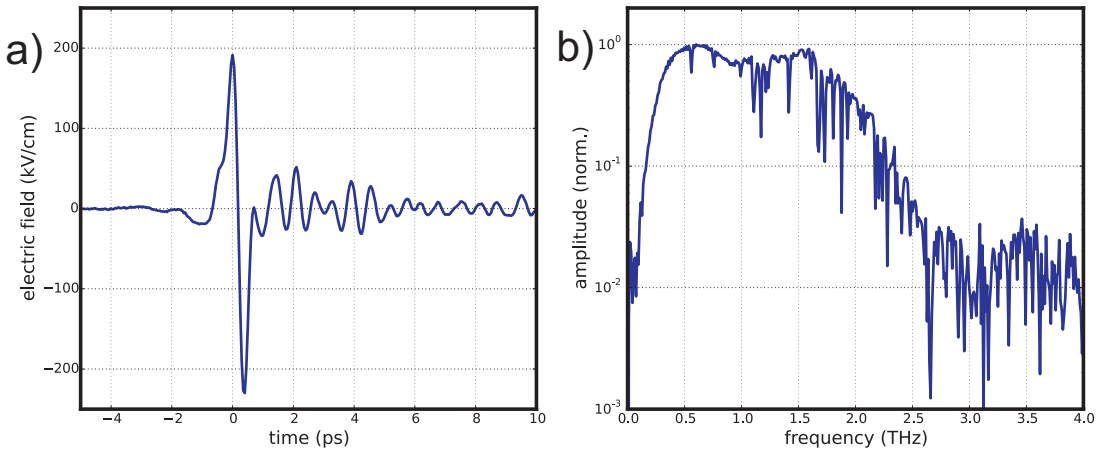

Figure 3.9: EO Sampling of the THz Pulse - a) The electric field in the time domain, measured in a GaP crystal. The pulse is approximately single-cycle, with a peak electric field reaching 230 kV/cm. Some of the oscillations after the peak of the THz pulse are due to dispersion in the generation and sampling crystals, while some is due to absorption and re-emission by water vapour. b) The amplitude spectrum, obtained by a Fourier transform of the time domain waveform. The spectrum is typically peaked between 0.6 and 0.8 THz, with frequency components up to 2.5 THz. The sharp dips in the spectrum between 0 and 2.5 THz match precisely with water absorption lines.

The fast fourier transform (FFT) of the time domain waveform is shown in fig. 3.9 b). The spectrum is peaked at around 0.7 THz, with a second maximum at 1.5

THz. This double peaked behaviour has been seen by other groups with TPFP THz sources(15). It should be noted that although this behaviour occurs with thick EO crystals due to dispersion, that is unlikely to be the origin of this behaviour here for two reasons: we are using a thin crystal (200 μm), and the spectrum does not change significantly when using a ZnTe crystal.

The main benefit of using a wafer stack, as described previously, is the ability to use a thin sampling crystal without introducing reflections spaced closely in time with the main pulse. This enables a very long baseline scan window without having to use post processing to remove reflections. As a result, the frequency spacing in the FFT is very fine and water vapour absorption lines(66), the sharp dips in the spectrum between 0 and 2.5 THz, are resolved with two to three data points per line. In a dry nitrogen environment, these would not be present.

3.3 THz Modulation of PL Experimental Layout

The high power beam from the 20% originally split off from the Legend is used to photoexcite samples simultaneously to the intense THz pulses from the source described in the previous section. The photoexcitation beam size is reduced by a factor of 3 using a telescope arrangement with 30 and -10 cm focal-length lenses. The beam is then focused through a hole drilled in the first focusing parabolic in the THz beam path, shown in fig. 3.7. The knife edge method for spot size measurement is used, where the beam power is measured while translating a sharp edge through the spot. Assuming a Gaussian pulse, the resulting curve of P vs x (power vs knife edge position) can be fit using,

$$P(x) = \frac{P_0}{2}\left[1 - erf\left(\frac{\sqrt{2}(x - x_0)}{w_0}\right)\right], \tag{3.9}$$

where P_0 is the incident power, $x - x_0$ is the knife edge location relative to the center of the pulse, and w_0 is the intensity beam waist, or e^{-2} radius. From this measurement, the w_0 at the sample was found to be 0.3 mm.

The location of the THz focus is found by positioning a 1 mm aperture in the beam path and translating it to maximize transmission as measured by EO sampling. The photoexcitation beam is then aligned to the center of the aperture to fix the spatial overlap of the two pulses. The temporal overlap, t_0, is fixed by introducing a known delay into the pulse using a combination of the rough and fine delay stages, and can be found in two steps. First, a fast photodiode can be used to find t_0 to within a nanosecond. Second, by monitoring the transmission of the THz pulse through a GaAs wafer while translating the stages. The creation of free carriers results in a significant drop in THz transmission and t_0 can be found to within a picosecond. To obtain better accuracy it is necessary to make a measurement with a more instantaneous response such as EO sampling.

PL from the photoexcited sample is collected using a 1" diameter, 75 mm focal length lens with anti-reflection (AR) for 650-1050 nm. The lens is at approximately a 45° angle from the normal to the surface, i.e, PL is collected non-collinearly. An identical lens is used to focus the light onto a 1 mm optical fiber. For integrated PL, the light is routed to a large area Si photodetector (Thorlabs, PDA100A).

The THz generation beam is modulated at 500 Hz with an optical chopper to facilitate the use of a lock-in amplifier (SRS SR830). The differential PL and absolute PL were acquired simultaneously by using two lock-ins, one set to the first and one to the second harmonic of the chopper. The time constant was typically set to either 100 or 300 ms, on normal reserve with both the LINE and 2x LINE filters activated, and the sensitivity varied from experiment to experiment.

For spectrally-resolved PL, the fiber is coupled to a monochromator (Princeton Instruments) with both single-channel (using an APD) and multi-channel (using a CCD) capabilities. In the single channel mode, the output of the APD (Menlo APD210) was fed to a boxcar integrator (SRS SR250), as the signal was too fast to be measured directly by the lock-in amplifier. The DC voltage measured output by the boxcar integrator, set to the "last sample" setting, was sent both to a lock-in amplifier to measure the differential PL and directly to the DAQ (the voltage output was between 0 and 1

V) to measure the absolute PL.

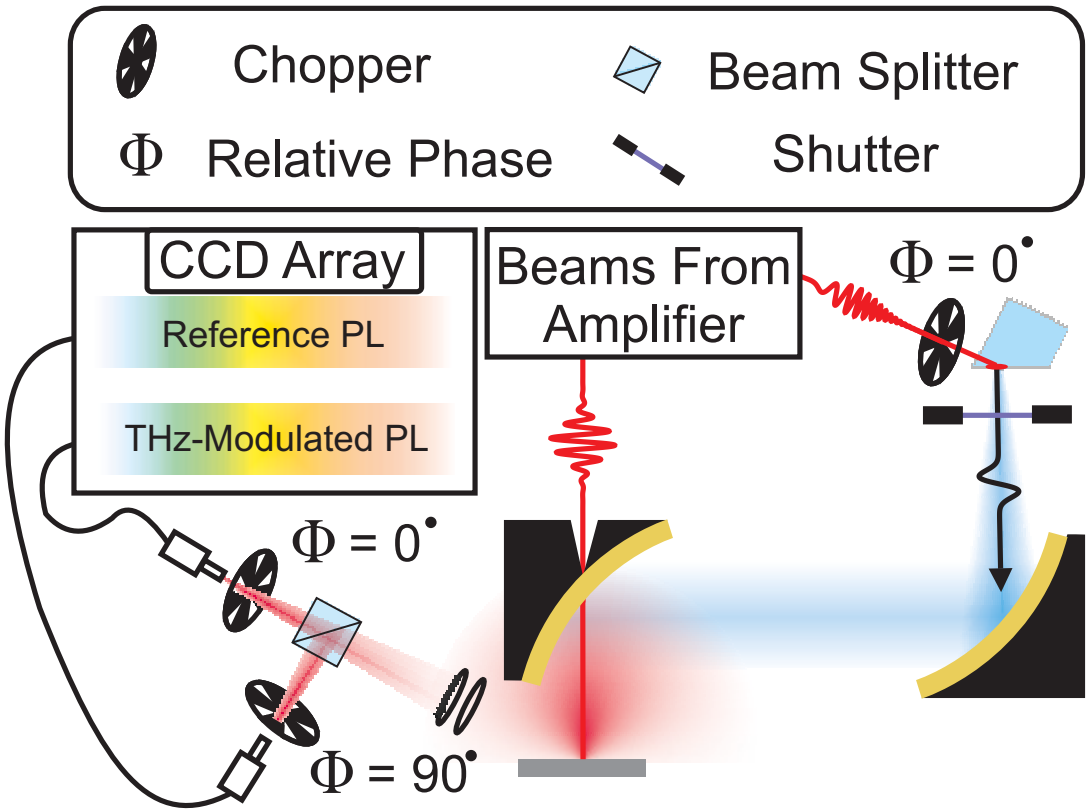

Figure 3.10: Parallel detection of THz-ΔPL - PL is collected and focused through a beamsplitter onto two fibers that are part of a bundle. One is chopped in phase with the THz pulse, and one 90° out of phase. The bundle is routed to the entrance slit of a spectrometer. The grating disperses light in the horizontal direction, but the vertical dimension is imaged 1 to 1 onto a CCD array so that the reference and THz modulated PL are spatially separated. An electronically controlled shutter is placed after the THz generation crystal and closed to obtain a calibration between the two channels.

Alternatively, the CCD array could be used to parallelize the measurement. The PL itself was not stable enough to do a multishot measurement first with the THz on, averaging over several seconds to acquire a reference, and then with the THz off to collect a background. Instead, a technique to simultaneously acquire a reference and modulated spectrum was devised, shown in fig. 3.10. A 50-50 cube beam splitter feeds PL collected from one of the two collection points into the inputs of an 2-to-1 optical fiber bundle (Thorlabs) that is connected to the spectrometer. The input to

each channel is chopped at 500 Hz.

One of the choppers is in phase, and one 90° out of phase with the THz chopper such that one channel saw the reference spectrum and the other saw the THz-modulated spectrum. This technique allowed for rapid acquisition of 2D scans, measuring the differential PL as a function of both wavelength and time delay. A calibration between the two channels can be made by acquiring a spectrum with the THz beam blocked. As the transmission and reflection of the beamsplitter was not flat as a function of wavelength, the PL signal from each channel is first added together, and a calibration coefficient is obtained separately for each channel,

$$I_{TOT} = I_A + I_B, \tag{3.10a}$$

$$\sigma_A = \frac{I_{TOT}}{I_A}, \tag{3.10b}$$

$$\sigma_B = \frac{I_{TOT}}{I_B}, \tag{3.10c}$$

where I_{TOT} is the total PL, $I_{A,B}$ are the PL from each channel, and $\sigma_{A,B}$ is the resulting calibration coefficient to be applied in post processing. At high fluences, the system was still susceptible to noise. An automated calibration scheme was used, where an electroncially activated shutter was used to block the THz generation beam immediately after generation, and acquire a calibration dataset before each measurement of the THz modulation.

4

THz Modulation of Photoluminescence

Having introduced the fundamentals of semiconductor physics and the details of the experimental set up, we now turn our focus to the experimental results. The layout of the experiment is shown schematically in fig. 4.1, where an intense THz pulse and optical pulse with delay Δt are incident on a semiconductor. Here, positive time implies that the optical pulse arrives first. Luminescence is collected and monitored for changes induced by the THz pulse (THz-ΔPL).

A previous studies have shown THz-pulse-induced photoluminescence quenching (THz-PLQ) of 4% in GaAs and 17% in cadmium telluride (CdTe) with an unmodified spectral line shape(67). Here, the quoted optical pulse excitation parameters are 0.01 mW excitation power with a 0.05 mm spot size, and the THz field was measured to be 100 kV/cm. No change in PL was observed in ZnSe, ZnTe, or GaP, where the carriers are generated with large excess energy(67). The PLQ was attributed to THz-induced heating, but the precise mechanism was not elaborated.

Chu *et al.* studied these results further using Monte Carlo methods to study the number of intervalley phonons emitted during the THz pulse(68). Each intervalley phonon was considered a non-radiative center and rate equations were solved to calculate the change in radiative efficiency. Agreement with experimental data was obtained over a range of excitation densities. However, in order to account for the magnitude of

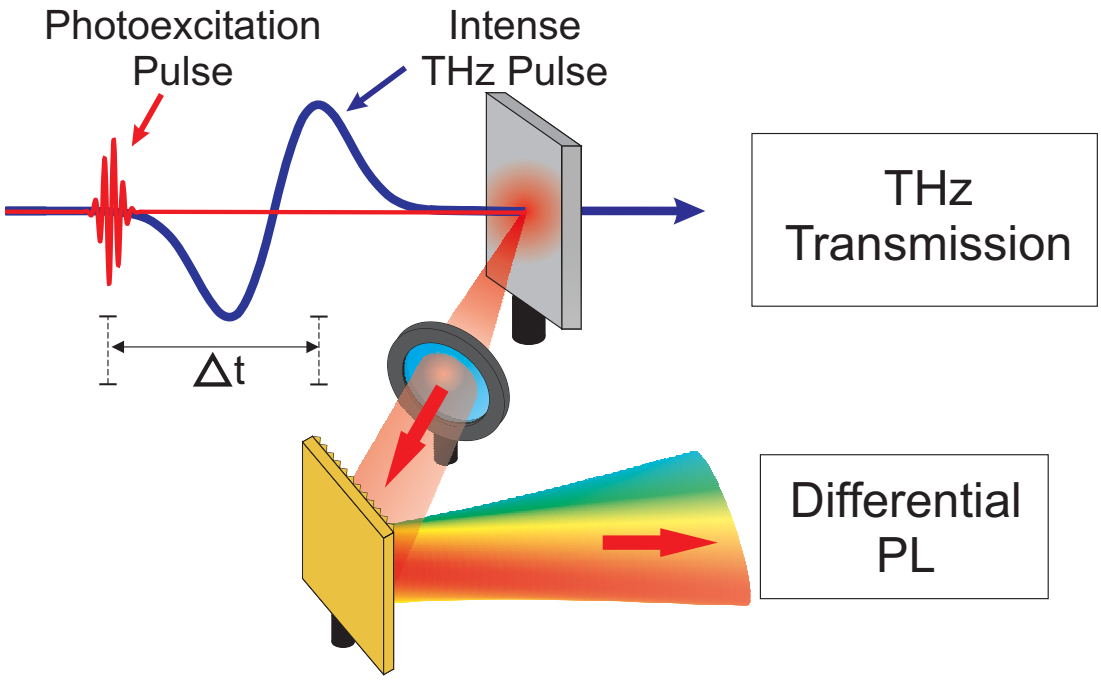

Figure 4.1: THz Modulation of Luminescence - An intense THz pulse is normally incident on a semiconductor collinearly with an 800 nm femtosecond pulse at a variable time delay. Here, the THz pulse is considered the pump beam, so that negative time implies that the optical pulse arrives before the THz pulse. PL is collected at approximately a 45° angle, and the THz-ΔPL is monitored with a CCD, or photodiode and lock in amplifier.

quenching, high rates of non-radiative recombination must be assumed.

However, this problem has not been studied further, despite the lack of clarity and technological relevance. Here, we explore the THz modulation of PL over a variety of excitation densities and THz energies in the semiconductors GaAs and InP. Some of the experimental results of ref. (67) are confirmed, and integrated THz-PLQ is observed as before.

More interestingly, we have discovered that intense THz pulses enhance light emission from the hot electron tail (THz-PLE). With increasing excitation density, a dynamic interplay between luminescence quenching and enhancement occurs, resulting in a density-dependent integrated change in luminescence. At high fluences, adjustment of the laser compressor can actually lead to integrated THz-PLE.

	GaAs	InP		GaAs	InP
E_Γ (eV)	1.42	1.34	m^*_Γ	0.067	0.072
E_L (eV)	1.71	1.93	m^*_L - l, t	1.91, 0.076	1.82, 0.132
E_X (eV)	1.90	2.19	m^*_X - l, t	1.28, 0.24	1.35, 0.275
E_{SO} (eV)	-0.34	-0.11	γ_1, γ_2, γ_3	7.03, 2.33, 3.03	6.64, 2.10, 2.81

Table 4.1: Band Parameters - The band parameters for GaAs and InP. Energies are given for the 3 minima in the first conduction band, measured from the top of the valence band. The Γ valley effective mass, m*, is isotropic, while the satellite valleys are not. The longitudinal and transverse (l and t) effective masses for the satellite valleys are quoted. The Luttinger parameters, γ_n, from which all hole effective masses can be calculated, are quoted. All data is taken from Saidi et al. where a 40 band **k·p** method was used to calculate the bandstructure(20).

4.1 Sample Details

GaAs and InP are III-V direct-gap semiconductors with zinc-blende crystalline structure. Both have bandgaps in the NIR of 1.42 eV and 1.34 eV for GaAs and InP respectively. The conduction band minima is at the Γ point, with satellite valleys at the L and X points. There are three valence bands which we will consider, the lh, hh, and SO bands. The band parameters are summarized in tab. 4.1.

The samples used in this study were [100] undoped GaAs, and [100] undoped InP (MTI Corporation). The quoted mobilities were similar, on the order of 5000 $cm^2/V \cdot s$. The quality of the GaAs wafer was very high with a quoted carrier concentration of $\rho < 10^9$ cm^{-3}, while the carrier concentration for the InP wafer was above $\rho = 10^{15}$ cm^{-3}. In InP, THz reflections from the backsurface of the crystal were suppressed relative to GaAs, likely due to free carrier absorption.

In an attempt to suppress these backreflections in GaAs, stacked wafer structures were used. Two wafers were pressed together with a thin layer of vacuum pump oil in between. As a result, the reflections were spaced further apart in time. Although this worked to a certain extent, the wafers tended to delaminate over time, and it was not possible to obtain a self consistent data set using this method. InP was therefore the more desireable sample in some circumstances.

With a photoexcition pulse centered at 800 nm (1.55 eV) carriers are excited directly to the Γ-valley with insufficient energy to scatter directly to the L valley. Excitation in GaAs is exclusively from the lh and hh bands, as there is insufficient energy to excite from the SO band, while excitation from the SO hole band is possible InP. The THz-ΔPL is qualitatively similar in GaAs and InP, suggesting that mechanisms involving SO hole dynamics are unlikely to contribute significantly to these results, thus the SO band will not be discussed further.

An example of a PL spectrum from GaAs and InP is shown in fig. 4.2, taken at similar fluence. The two spectra are very similar, displaying the characteristic asymmetric lineshape of a direct-gap semiconductor(32). As the lattice temperature and effective masses are similar, the larger FWHM could be due to the extra electron excess energy on excitation (0.2 eV in InP vs. 0.1 eV in GaAs). Note the absence of a peak at 1.55 eV, the laser energy. The non-collinear luminescence collection geometry allows for the luminescence to be collected without being overwhelmed by the light from the laser pulse. Care was taken to find a clean portion of the sample surface to avoid scatter.

In both materials, the peak of the PL spectrum is located at the bandgap energy, with emission photon energies extending into the forbidden gap. The origin of luminescence with sub-band-gap energies is ubiquitous in semiconductors. At low temperatures, sub gap luminescence can be due to excitonic effects or impurity luminescence(69), however at room temperature the origin is not as obvious. Some studies correlate the sub-gap PL with band tail states, e.g., the Urbach tail(70), while others attribute it to many body effects(43).

The TO (LO) phonon at zero wavevector are at 8.0 (8.5) THz in GaAs, and 9.2 (10.3) THz in InP(71). Based on the excess energy on excitation, 3-4 (GaAs) and 4-5 (InP) LO phonons are emitted per electron during relaxation. As a result, hot phonon effects, which keep the carrier distribution hot, are likely more prominent in InP(25).

The hot phonon effect is also amplified in InP due to the large phononic bandgap, as the zone edge acoustic phonon is at 5.8 THz in InP vs. 6.77 THz in GaAs. LO phonon relaxation is suppressed, as there are less decays which satisfy energy and momentum

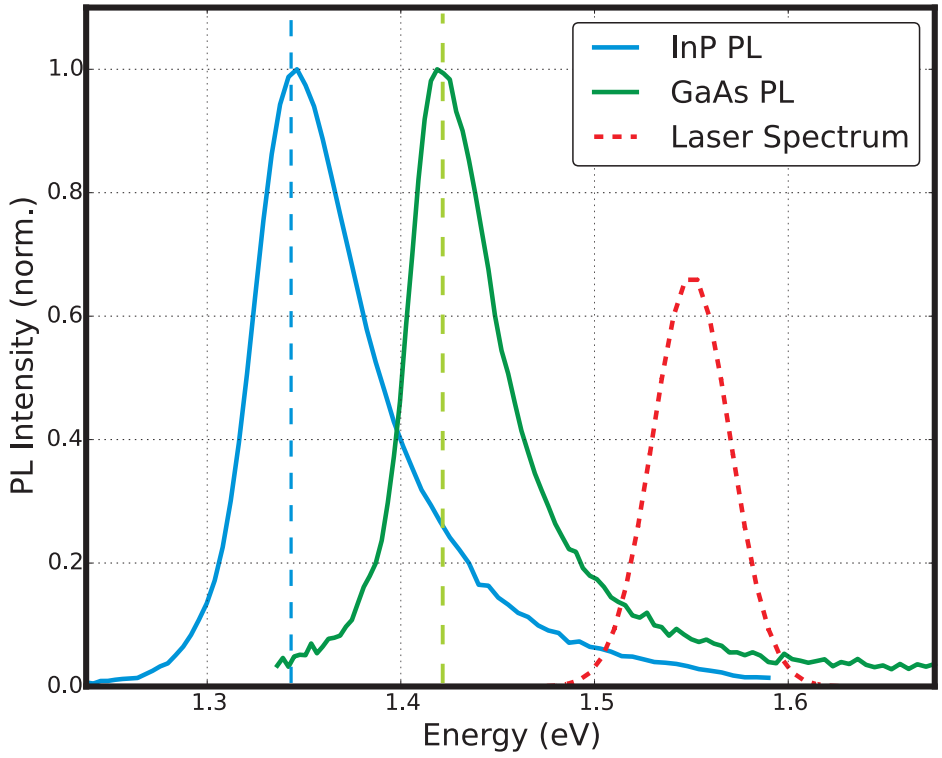

Figure 4.2: PL Spectra - The photoluminescence spectra of GaAs and InP at similar excitation fluences with a 50 fs, 800 nm pulse. Both show the characteristic asymmetric lineshape expected from direct-gap semiconductors. The luminescence spectra are peaked near the bandgap energies of 1.42 eV in GaAs (dotted green), and 1.34 eV in InP (dotted blue). In both, there is a significant amount of sub-gap luminescence, and a high energy tail extending beyond k_bT due to hot electrons.

conservation(72). This is apparent in the LO phonon lifetime of 7.6 ps in InP vs. 2.5 ps in GaAs(73).

Finally, the Frölich coupling constant, which represents the strength of the polar-optical coupling between electrons and phonons, is also much larger in InP ($\alpha = 0.15$) than GaAs ($\alpha = 0.067$). The Gunn field in GaAs is 5.3 kV/cm vs. 15 kV/cm in InP(37). High field transport is qualitatively much different for electric fields similar in amplitude to the Gunn field, however in our work the peak electric field of 230 kV/cm is significantly larger than either of these values.

4.2 THz-ΔL in GaAs

4.2.1 Low Excitation Density

Shown in fig. 4.3 is the THz-pulse-induced ΔPL in GaAs as a function of luminescence photon energy and THz-optical pulse time delay for a carrier density of approximately $6 \times 10^{18}\ cm^{-3}$, calculated assuming linear absorption. At this density, the system is degenerate, and carrier-carrier scattering redistributes electrons in momentum space on femtosecond timescales(31). The time-domain waveform of the THz pulse overlayed indicates the instantaneous field at the time of photoexcitation. While thermally-excited carriers are affected by the whole THz pulse, newly generated electron-hole pairs are only influenced by the field from Δt onwards.

It can be seen that there is PLQ at photon energies near the bandgap and PLE of the high energy tail. The effects occur almost exclusively when the photoexcitation pulse is incident simultaneously with the optical pulse. Here, the PL quenching-enhancment crossover, E_X, appears to be independent of time delay, Δt. At Δt=-1.9 ps, there seems to be a second peak in the PLQ which is larger than the noise level. This could be due to the second small peak in the THz waveform.

Fig. 4.4 a) is a cross section of the 2D scan taken at Δt=0, showing both the absolute PL change (blue), and the fractional PL change (red). The absolute magnitude of the PLQ is greater than the PLE, and the integrated THz-ΔPL is negative. However,

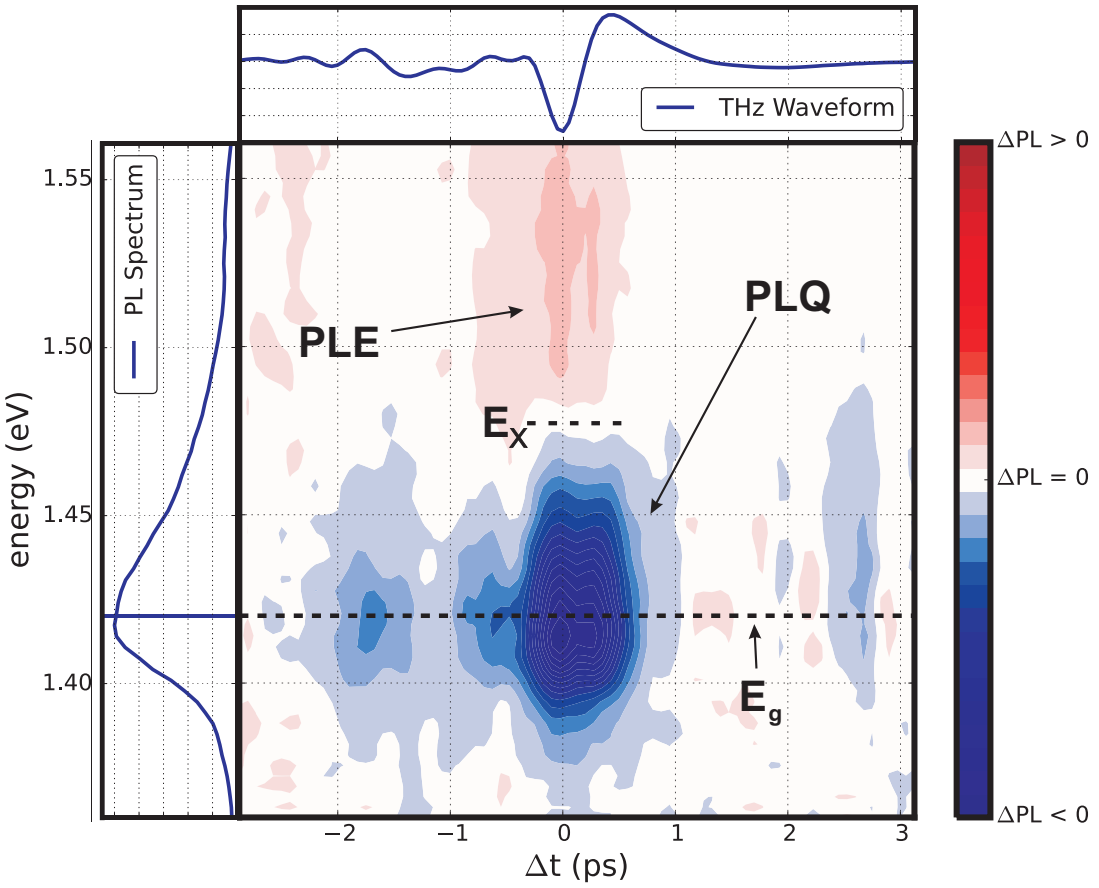

Figure 4.3: THz-ΔPL - Differential PL spectrum in GaAs as a function of THz-optical time-delay where positive delay implies the THz pulse (in our case the pump) arrives before the optical pulse. This was acquired by CCD detection, as described in chapter 2. Shown above is the THz electro-optically sampled waveform, and to the left the PL spectrum. Here, the crossover energy, E_X, is at approximately 1.48 eV.

the fractional change, $\Delta PL/PL$, of the enhancement is larger than the quenching as the magnitude of PL is much smaller at higher photon energies. The maximum modulation of quenching is approximately 4%, similar to that of Liu et al.(67).

The crossover energy between quenching and enhancement is located at approximately 1.48 eV, which is roughly $2k_bT$ at room temperature above the peak of the PLQ. This high energy PL is more likely to come at early times before the carrier distribution has cooled to the lattice temperature, implying that we are quenching some of the early time hot PL as well as that near the band gap. Some groups have reported hot carrier distributions which last for tens of picoseconds(74), and it would be very interesting to see how these dynamics are modified by intense THz pulses.

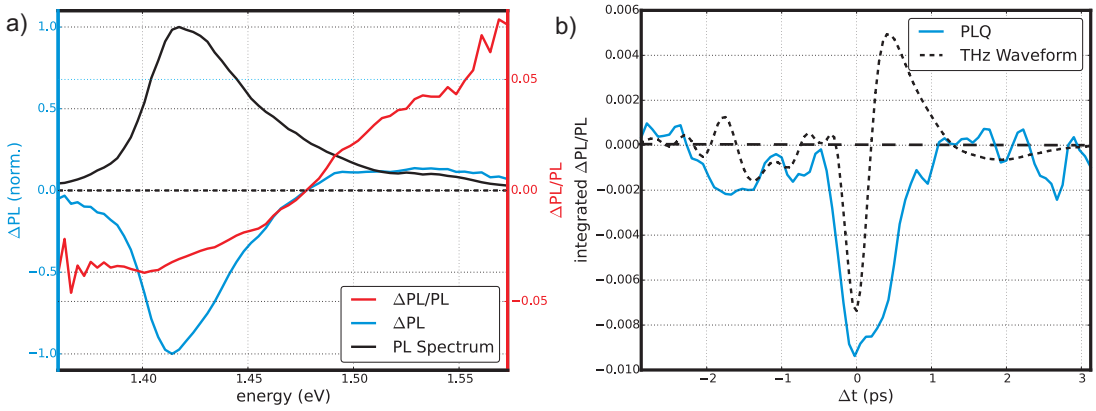

Figure 4.4: Temporal Cross Section - a) spectrally-resolved differential PL, taken at time delay zero. The blue curve shows the normalized absolute change in PL while the red curve shows the fractional change. The black curve is the normalized PL spectrum, for reference. The absolute change is dominated by PLQ, while the fractional change is dominated by PLE. b) The integrated fractional change in luminescence, obtained by integrating across the spectrum, with the THz pulse overlayed for reference. A peak modulation of 0.9% occurs when the optical pulse is coincident with the peak of the THz pulse. If the delay is approximately 1 ps in either direction, very little modulation occurs.

The integrated THz-ΔPL was extracted from fig. 4.3 by integrating the differential spectrum for each time delay, shown for each time delay fig. 4.4 b). There is an overall reduction in luminescence of almost 1%. Assuming an initial radiative efficiency of 20%, which is a reasonable estimate based on excitation parameters(75), this means that approximately of 10^{16} cm^{-3} additional carriers recombine non-radiatively over the

course of relaxation.

In fig. 4.5 we studied the THz energy dependence of this phenomenon, with the excitation density set similar to the results in fig. 4.3. In a), the THz energy is varied using wiregrid polarizers and the fractional change in PL is measured using a lock-in amplifier. The magnitude of quenching scales linearly with the energy . In b), the spectrally-resolved ΔPL is shown for 3 different energies. The lineshape and crossover point seem to be independent of THz energy.

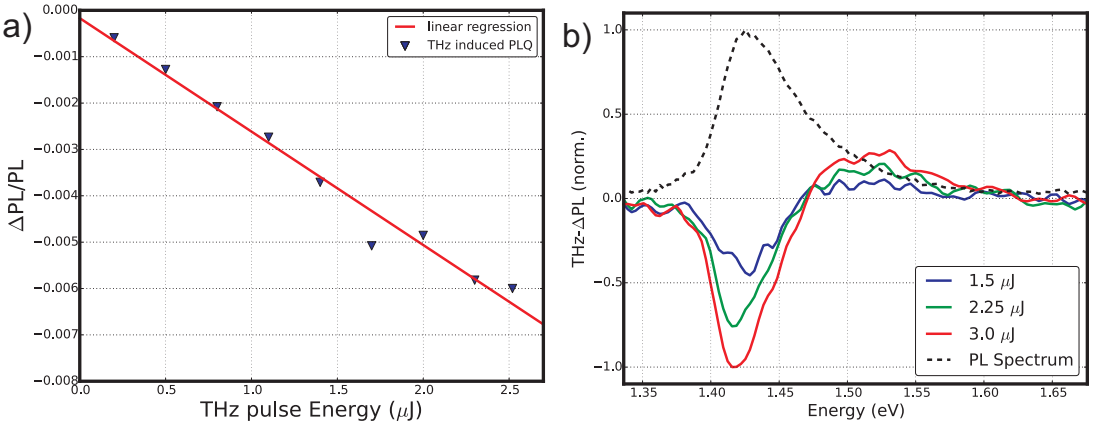

Figure 4.5: THz Energy Dependence - a) Integrated THz-PLQ in GaAs measured with a photodiode as a function of THz energy, showing a linear trend. b) Spectrally-resolved THz-ΔPL for three THz energies collected at the peak time delay using a monochromator and avalanche photodiode. The magnitude of each curve is normalized to the peak quenching for the 3.0 μJ case. The characteristic features of the differential curve, the lineshape, location of peaks and valleys, and crossover wavelength remains essentially unchanged as a function of THz energy.

4.2.2 Increasing Excitation Density

Shown in fig. 4.6 a) is the integrated THz-ΔPL as a function of pump power for several carrier densities at the peak time delay. The relevant excitation parameters are summarized in table 4.2. In fig. 4.6, both the absolute (blue) and fractional(red) PL change are plotted. The qualitative behaviour of the two curves is different. While with increasing excitation density the magnitude of the fractional modulation monotonically decreases, the absolute change first grows and then shrinks, i.e., there is two

Pump Power (mW)	Carrier Density ($\times 10^{18}\ cm^{-3}$)	Quasi Fermi Level (meV)
0.13	0.96	53
0.4	3.0	110
0.71	5.3	160
1.07	7.9	220
1.35	10	250
1.84	14	310
2.35	17	370
2.84	21	410
3.34	25	460
3.91	29	510
4.5	33	560
5.26	39	630
6.1	45	690
7.0	52	760

Table 4.2: Excitation Parameters - The pump power, carrier density, and quasi-Fermi level for each data point in fig. 4.6. The carrier density estimates are made assuming linear absorption. This assumption must break down, as the calculated quasi-Fermi level has reached the level at which electrons are injected into the system. The quasi-Fermi level was calculated by inverting eq. 2.7 with parabolic bands and 0 temperature. The high-T calculation results in a Fermi-level which is several meV lower.

qualitatively different regimes as a function of photoexcited carrier density.

The corresponding the differential spectra for the first several pump powers are shown in fig. 4.6 b). The PLQ-PLE crossover energy, E_X, shifts towards lower energies, and the magnitude of both the PLQ and PLE increases as the pump power increases. However, at 1.35 mW, the power where the integrated absolute modulation begins decreasing both of these trends change. The crossover energy does not change significantly and the amplitudes decrease.

At this point, it is useful to see if there are any trends in the unmodulated PL spectra. Shown in fig. 4.7 a) is the integrated PL as a function of pump power measured for each pump power in table 4.2. At very high power the data shows a sub linear increase. This could be due to the onset of Auger recombination(76). The inset shows the same data with only the first four datapoints. In this regime the PL shows a superlinear increase in luminescence. At this excitation fluence, the quasi Fermi levels of electrons

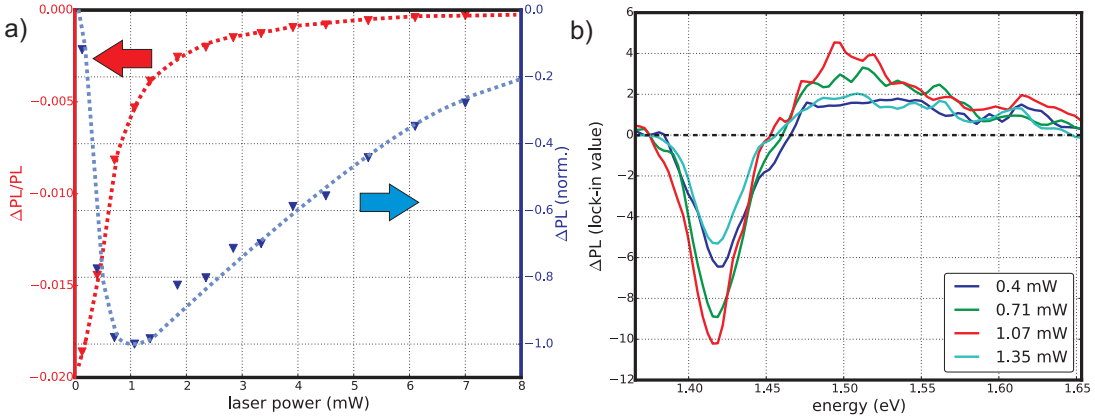

Figure 4.6: THz-ΔPL Pump Power Dependence - a) The peak absolute (blue) and fractional (red) change in integrated PL, measured as a function of laser pump power in GaAs. While the magnitude of the fractional modulation is monotonically decreasing, the magnitude of the absolute modulation first increases rapidly, then decreases. b) Differential spectra for the first four pump fluences. The general trend is a shift of E_x towards the bandgap with increasing power, and an increasing magnitude of both quenching near the gap, and enhancement of the high energy tail. At 1.35 mW, the trend no longer continues, and the amplitude of both the quenching and enhancement decreases.

and holes are within their respective bands, thus, the superlinear increase could be due to the onset of stimulated emission. However, the superlinear trend only holds for two data points in this dataset.

Another interesting trend in the PL can be seen by studying the normalized spectrum which is shown in fig. 4.7 b). With increasing excitation power, the spectrum begins to narrow. This spectral narrowing can also be indicative of stimulated emission(77). Typically, increased pump power leads to a broadening of the PL spectrum(78).

However, there is another possible interpretation of the spectral narrowing. At high densities, absorption bleaching increases the penetration depth of the optical pulse. A larger fraction of carriers are generated deeper in the bulk of the semiconductor, and it becomes more difficult for photons to leave the material. Photon re-absorption would lead to a redshifting of the PL spectrum. Additional data at low pump fluence examining the superlinear increase in PL is necessary to corroborate the stimulated emission conclusion.

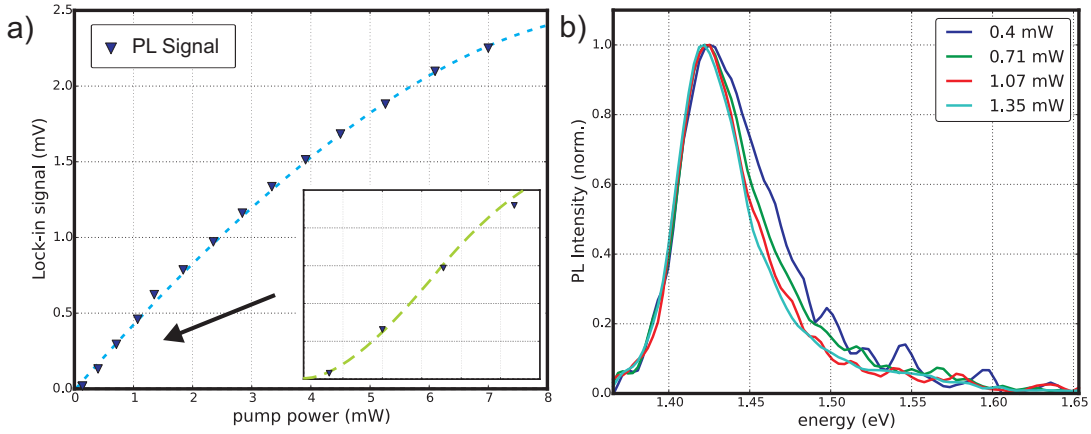

Figure 4.7: Absolute PL signal - a) The PL intensity in GaAs as a function of excitation power, measured with a photodiode and lock-in amplifier. The general trend is a sublinear inrease in PL, possibly due to the onset of Auger recombination. The inset is a magnified version of the first four datapoints. For the first two points, the PL seems to increase superlinearly with pump power, which could be an indication of the onset of stimulated emission. The green and blue dotted curves are lines drawn as a guide to the eye. b) The corresponding PL spectrum for 4 pump powers in the superlinearly increasing regime, acquired with the monochromator and APD. The spectrum for the lowest power was not plotted, as the signal was to low to acquire. The trend is a narrowing spectrum and a slight shift of the peak to lower energies. The trend of spectral narrowing and red shift continues as power is increased, however more gradually (not shown).

4.2.3 High Fluence Regime

At high pump powers a qualitatively new feature develops. The integrated THz-ΔPL as a function of time delay shows PLE when the THz pulse arrives before the optical pulse, as seen in fig. 4.8. In this long baseline scan, there are three separate components to the THz-ΔPL, 1) the main peak, when the THz pulse and optical pulse are incident on the semiconductor at the same time, 2) when the THz pulse reflected from the back surface reaches the front surface simultaneously to the optical pulse, and 4) off t_0 behaviour when neither the incident, nor back surface reflected pulses are coincident with the optical pulse. This scan was taken at 1.5 mW.

It is curious to note that the amplitude of THz-PLQ from the backsurface reflected pulse is almost as large as that of the front surface. It is unexpected as the electric field of the THz pulse is significantly reduced after reflection from the back surface. This behaviour, where stronger nonlinear effects are seen with back surface illumination, has been seen before in studies of THz induced transient voltage pulses in doped semiconductors(62), as well as in studies of THz-induced photoemission from plasmonic antennae(79).

In fig. 4.8, wafer stacks were used to separate the backreflection further in time from the main pulse. At the moment, there is no clear interpretation of the off t_0 effects. The high quality of the wafer, indicated by the low intrinsic carrier concentration, could mean that some carriers excited from the previous photoexcitation pulse have diffused into the bulk and have not recombined(80). This could be some sort of interaction between photoexcited carriers left over from the previous pulse.

The THz-ΔPL also becomes strongly dependent on the compressor setting of the excitation pulse. Shown in fig. 4.9 is the integrated THz-ΔPL near t_0 for 3 different compressor settings with the direction of the chirp indicated by the inset. When this dataset was taken, there was also no method in place to quantitatively measure the amount of pulse chirp. 4.9 a), b), and c), correspond to compressor settings which gave approximately 50% of the maximum SHG, maximum SHG, and 50% of the maximum

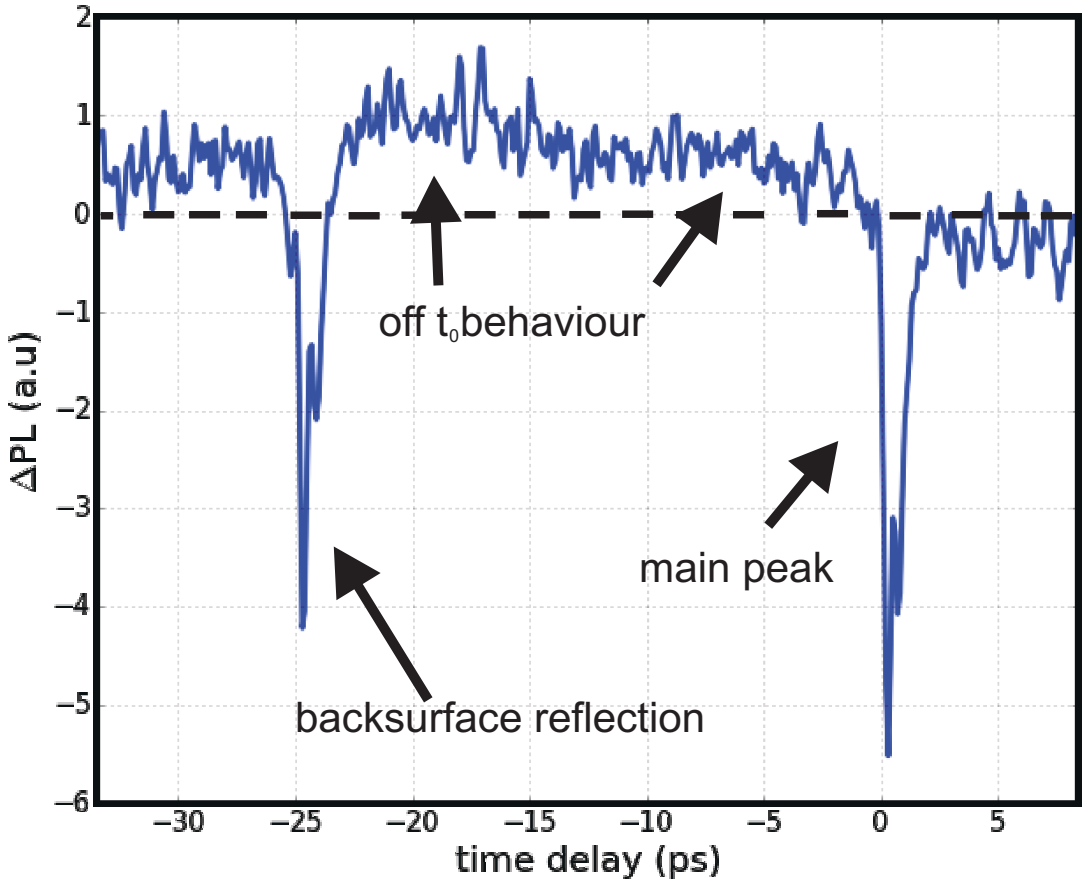

Figure 4.8: Long Baseline Scan - THz-ΔPL in GaAs at 1.5 mW. The peak at 0 ps is t_0 for the incident pulse while the peak at -25 ps is t_0 for the back surface reflection. There is also an element of off-t_0 integrated enhancement.

but with the opposite chirp, respectively.

All three curves in fig. 4.9 show a positive offset, integrated THz-PLE, at negative time due to the off t_0 effects. In the chirped pulse cases, there is strong integrated PLE near t_0. In other datasets, there was indications that the behaviour was asymmetric about the minimum pulse duration. This could be due to the cubic phase of the excitation pulse as discussed in chapter 2.

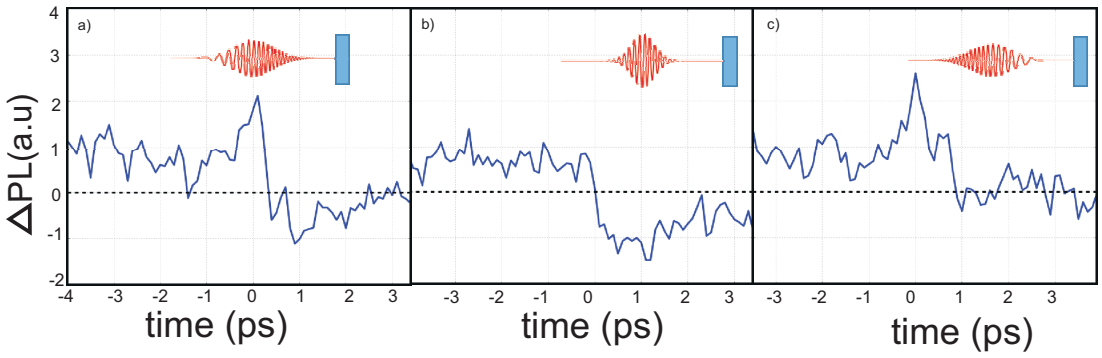

Figure 4.9: Chirp Dependence - THz-ΔPL in GaAs for 3 different compressor settings, corresponding to a) down chirped, b) minimum pulse duration, and c) up chirped. The direction of chirp is indicated schematically in the inset of each figure. The minimum pulse duration was set by maximizing SHG from a BBO crystal, and the up and down chirp cases were chosen as the position where the SHG intensity was approximately half the maximum value. When the pulse is chirped, and the photoexcitation and THz pulses are coincident, there is a large THz-induced PLE.

4.3 THz-ΔL in InP

The THz reflections present in GaAs were absent in InP due to the high intrinsic carrier density, as evidenced by fig. 4.10, displaying only as single PLQ peak in an 80 ps window. Qualitatively, the behaviour of the THz-ΔPL signal is very similar to that of GaAs and exhaustive study will not be presented. The integrated PLQ scales linearly with THz energy at low fluence, and the percent PL modulation decreases with increasing optical fluence. The quenching-enhancment crossover energy, E_X, shifts towards the bandgap and the PL spectrum narrows with increasing pump fluence.

While most of the results were qualitively similar in the two semiconductors, the lack of back surface reflections meant that the off t_0 effects seen in GaAs were not present in InP. This made the sample more ideal for studies of the high fluence regime chirp dependent effects. We studied the THz energy dependence of the PLQ and PLE in the spectrally-resolved data, shown in fig. 4.11.

This data was obtained with the monochromator and avalanche photodiode at a pump power of 1.5 mW. While the quenching scales linearly with energy, the enhancement does not. This is different from the low fluence regime where both the quenching

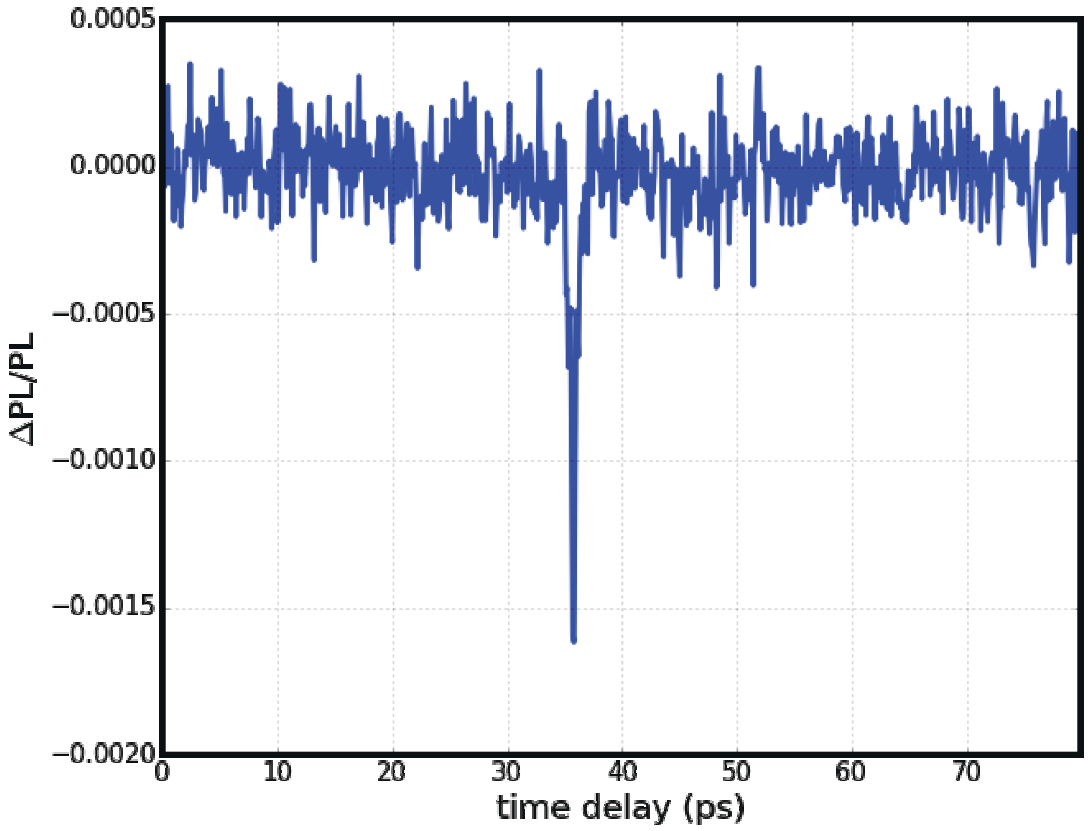

Figure 4.10: THz-ΔPL in InP - A long baseline integrated THz-PLQ scan in InP.The 80 ps window shows a lack of reflections, making this sample more ideal for the study of THz-ΔPL in the high fluence regime.

and enhancement scale linearly.

In the high fluence regime, the THz-ΔPL shows a dependence on laser pulse compressor setting, as shown in fig. 4.12. Interestingly, as the amount of chirp is increased the integrated behaviour shows both PLQ and PLE in the same time delay scan. It appears as though when the optical pulse is coincident with the leading peak of the THz pulse there is PLQ, while when it is coincident with the trailing half of the THz pulse there is PLE 4.12.

We also studied the spectrally-resolved ΔPL for each of the three compressor settings from fig. 4.12. The results are shown in fig. 4.13. Here, it was difficult to make a proper comparison between the three spectrally resolved datasets as changing the

compressor setting changed the stage position of t_0. The stage position was chosen as the location with the maximum amplitude of integrated PLQ. The blue, green, and red curves correspond to figs. 4.12 a) to c) respectively. By changing the compressor setting, the lineshape of the differential PL is changed.

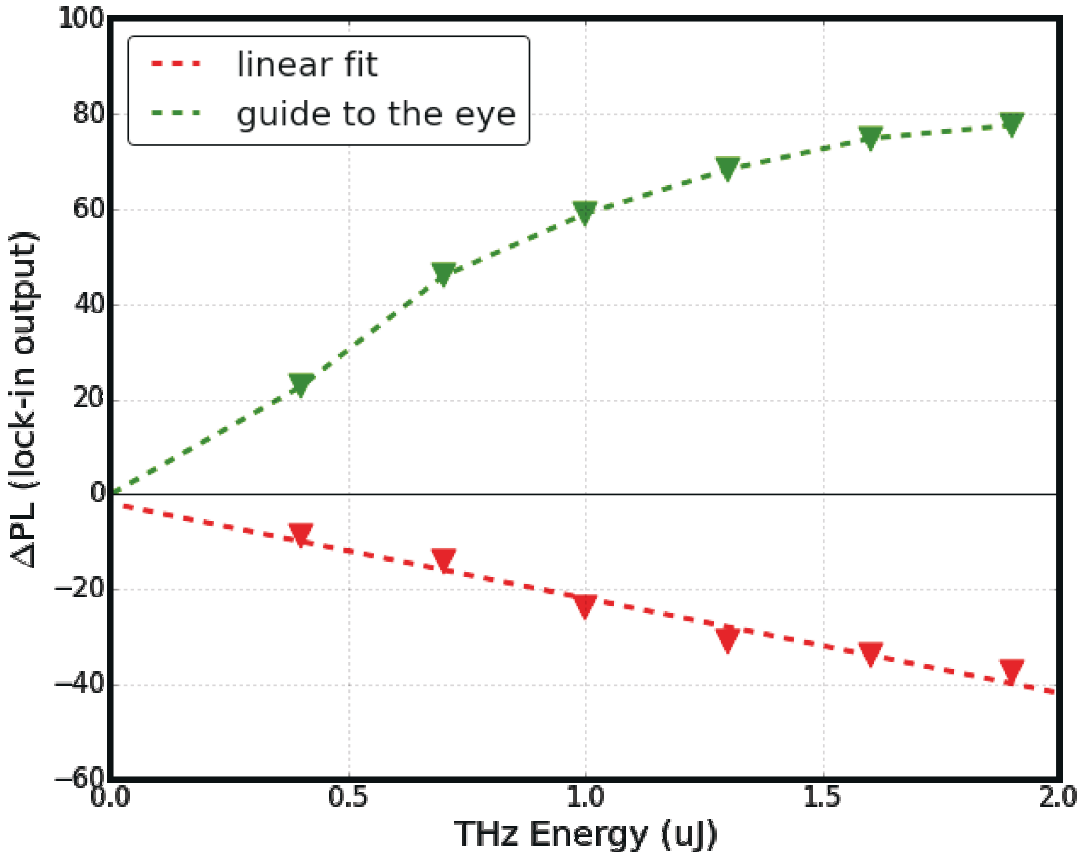

Figure 4.11: Spectra THz Energy dependence - Total PLE (green) and PLQ (red) in InP at 3.0 mW pump power, obtained by integrating over the positive (enhancement) and negative (quenching) regions in the spectrally-resolved data, as a function of THz pulse energy. The integrated PLQ seems to scale linearly with THz energy as indicated by the linear fit, while the enhancement shows nonlinear behaviour. The green line is drawn as a guide to the eye, to highlight the sub linearity of the trend. Here data was collected with an avalanche photodiode and monochromator, and scans were averaged until the trace converged.

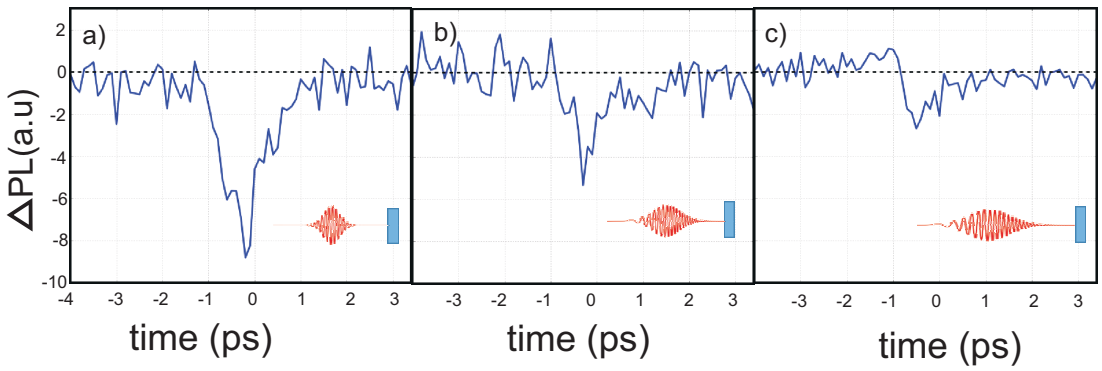

Figure 4.12: Integrated Chirp Dependence - The integrated THz-ΔPL in InP for three different compressor settings at 3.0 mW pump power. a) Minimum pulse duration set by maximizing SHG in a thin BBO crystal, b) a small amount of down chirp corresponding to 50% of the maximum SHG, c) a large down chirp correpsonding to approximately 25% of the maximum SHG. The direction of chirp is indicated schematically in the inset.

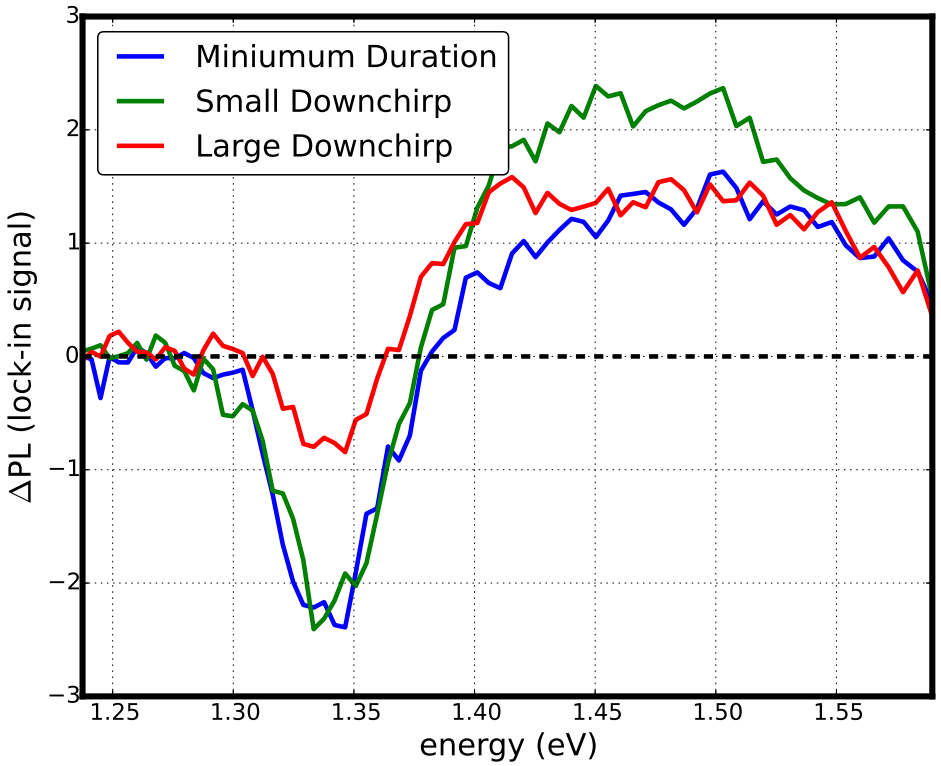

Figure 4.13: Spectrally-Resolved Chirp Dependence - Spectrally resolved THz-ΔPL in InP at 3.0 mW pump power for three different compressor settings. The lineshape changes dramatically for each case. Here, the compressor settings were chosen as the locations where SHG was maximized, half maximum, and one quarter maximum for the minimum, small downchirp, and large downchirp cases

Chapter 5

Discussion

We have shown that intense THz pulses modulate both the luminescence intensity and lineshape in the direct-gap semiconductors GaAs and InP. A wide range of excitation conditions have been explored and in general it is seen that THz pulses enhance high energy PL and quench near gap PL. In almost all conditions quenching dominates. However, with high density excitation and chirped optical pulses the enhancement can overwhelm the quenching.

Several reports of intense THz pulse effects on luminescence exist in a variety of systems. Shinokita et al. showed THz-PLE in undoped GaAs quantum wells under CW excitation, and attributed it to ionization of trap states at interfaces(81). Also in quantum wells, Rice *et al.* observed transient quenching of excitonic luminescence in quantum wells with THz pulses tuned to the the 1s-2p excitonic transition(82). Interestingly, they also saw simultaneous enhancement of 2s luminescence, from Coulomb mediated transitions from the 2p to 2s states. In bulk GaAs, metamaterial enhanced THz fields on the order of tens of MV/cm have been shown to induce interband Zener tunneling, resulting in luminescence(15). However, none of these results can be used to explain the THz modulation of luminescence presented here. The first and the third both exhibit complex electric field dependence which is different from the linearity observed here. The second requires the presence of an exciton population, which is unlikley at high temperatures.

In another context, researchers have explored the THz-pulse-induced Franz-Keldysh effect, which is the modification of the semiconductor absorption coefficient by an electric field. In these experiments, the time delay data showed similar behaviour to the THz-ΔPL. Here again, however, a complicated electric field dependence is expected(83). The linearity with increasing THz energy of the integrated PLQ, as well as the unmodified lineshape of the differential spectrum indicate that the THz-ΔPL we have observed is not an obvious manifestation of the Franz-Keldysh effect.

THz-PLQ has been studied before by Liu *et al.* and attributed to carrier heating, however no model was presented, and no THz-PLE was observed(67). Chu *et al.* developed a model to simulate the THz-PLQ using Monte Carlo simulations(68). Here, the interpretation of the effect is that intervalley phonons emitted due to carrier acceleration in the THz field act to enhance non-radiative recombination. Within this model, it is not clear whether intervalley phonons act as non-radiative centers themselves, or if they act to increase transition rates through the usual channels. The latter seems possible, as molecular dynamics simulations have shown that high-wavevector phonons couple more efficiently to lattice defects(84) and heat non-radiative centers.

In our results we have seen up to 2% reduction in PL in GaAs, and Liu et al. quote up to 17% in CdTe(67). In their model, Chu *et al.* assume that all modulation of luminescence occurs during the lifetime of the non-equilibrium phonons, which is just 2.5 ps for GaAs. A back of the envelope calcuation assuming an exponential decay puts the required rate of non-radiative recombination on the order of nanoseconds. For typical non-radiative centers trapping can occur on picosecond timescales(85), while emptying typically occurs on microsecond timescales(86).

While not entirely unreasonable, it is difficult to reconcile the large modulation of luminescence reported. It is useful to consider the indirect gap semiconductors germanium and silicon for comparison. The conduction band minimum for germanium (silicon) is at the L (X) point, where there are 4 (3) inequivalent minima. As a result, intervalley scattering can occur near the bottom of the conduction band, and it is the dominant relaxation mechanism during optical excitation. However, nanosecond

recombination times are not observed in these systems.

This evidence is not entirely convincing, and it is possible that this relaxation channel requires a non-equilibrium phonon population. The configurational coordinate diagrams introduced in chapter 2, and used to understand non-radiative recombination, is a highly simplified model. It is possible that the high effective temperatures of intervalley phonons open up new, efficient, channels for recombination. The hot phonon mechanism can also result in long lived non-equilibrium phonon. Hot phonons would also help explain the enhancement of high energy luminescence as phonon reabsorption keeps the electron distribution hot longer, and releasing more high energy PL.

One point which will be difficult to understand with this model is the fast switching time, i.e, there is essentially no modulation of luminescence with $|\Delta t| < 1$ ps. From previous studies, it is known that intense THz pulses can cause intervalley scattering long after t_0, at densities higher than 10^{18} cm^{-3}(65). In this case, it is not obvious why quenching does not occur at larger time delays.

Several interesting phenomenon occur at early times which could explain this behaviour. Ultrafast current surges due to built in surface fields, or current surge due to the difference between electron and hole effective masses (the photo-dember effect) result in charge separation(38, 39), which is known to reduce radiative efficiency. The strong electric field of the THz pulse leads to charge separation parallel to the surface, although it only lasts for several picoseconds(62). This transient charge separation alone is unlikely to account for the observed magnitude of quenching.

Alternatively, the THz-PLQ could be due to intervalley-scattering induced suppression of diffusion into the bulk during the initial current surge. This could hold carriers near surface where there is a high density of non-radiative states, increasing the rate of nonradiative recombination. It is possible to test this by chemically passivating the semiconductor surface, which significantly reduces the trap density(80), and should reduce the amount of luminescence quenching within this model.

Shifting focus, results with increasing excitation density point to the onset of stimulated emission in the PL spectrum. At liquid nitrogen temperature, stimulated emission results in rapid carrier density depletion by a factor of ten in just 20 picoseconds, at a carrier density of only 1.5×10^{18} cm^{-3}(87). While stimulated emission is suppressed at room temperature, there is likely still some contribution. It should be noted that even if the regime of optical gain is not reached, stimulated emission still results in an increased rate of recombination, enhancing radiative efficiency.

It is possible that THz pulse induced intervalley scattering could be suppressing stimulated emission by reducing Γ-valley population. In support of this conclusion, reports of sub-picosecond resolution luminescence studies in GaAs have shown a rise time of 10 ps when carriers are excited above the intervalley scattering threshold(88). By delaying light emission, the peak intensities required for stimulated emission to occur may not be reached, nulling the enhanced radiative efficiency which comes along with stimulated emission.

In general, the rate of stimulated emission depends on the elecron and hole quasi-Fermi levels, and the temperature(77), with lower temperature and higher Fermi levels resulting in more stimulated emission. The initial hot carrier temperature is dependent on the excess energy on excitation(78), so a lower initial temperature is expected for CdTe, vs GaAs, vs InP. This correlates well with the observed ratios of luminescence quenching, with CdTe being the highest reported, and InP the lowest as we have observed.

Still, based on our current results there is no smoking gun evidence pointing to the correct mechanism. From an experimental perspective, it would be interesting to explore the low fluence regime and low temperatures. If the THz-PLQ is due to suppression of stimulated emission, there would be no modulation at low fluence, and alternatively very large modulation at low temperatures. The low fluence regime should also shed light on the phonon-defect coupling model of Chu *et al.* as at low enough excitation fluences intense THz pulses will induce intervalley scattering long after t_0, which should manifest in the time delay data.

To extend these interpretations to the high fluence and chirped-pulse regime may be difficult. The quasi-Fermi level calculated from linear absorption is approaching the level of excess energy on excitation, and nonlinear absorption due to the Burrsein-Moss shift is important(89). Pulse compression begins to effect absorption and the distribution of carriers as a function of depth is different from that of linear absorption(90).

Additionally, Auger decay begins to dominate the recombination dynamics at carrier densities above $10^{19}\ cm^{-3}$(76). Here, it is possible that the reduction of density in the Γ-valley due to intervalley scattering reduces the rate of Auger recombination. An accurate model of initial carrier distribution, including nonlinear absorption, diffusion, and surface trapping, is likely required to understand these effects. As well, the compressor dependence of our results highlights the need for more accurate laser characterization, as discussed in chap. 2.

In this discussion, we have also ignored other interesting phenomenon which occur during the initial stages of excitation and relaxation. At low temperatures, unnexpected excitonic enhancement was seen in quantum wells during the first few picoseconds after exctiation(10). Some quantum-kinetic effects are important even at room temperature. When an electron-hole plasma is generated, a plasmon like response does not develop immediately and the couloumb interaction is unscreened. A fully correlated system forms on timescales of the inverse plasma frequency, in our case on the order of hundreds of femtoseconds for carrier densities on the order of $10^{18}\ cm^{-3}$(9).

Simultaneously, coherent phonons are excited by impulsive excitation(91). Very little work has been done studying the simultaneous coherent evolution of both the lattice and carriers. Recent work using time-and-angle-resolved photoemission spectroscopy have pointed towards novel physical processes which occur during the initial thermalization phase(92). Perhaps non-radiative recombination channels which are affected by the THz pulse are present in this regime. While without precedent, these exciting possibilities are worth considering, as they could point towards new physics.

Here we have presented a study of these effects for a wide range of conditions. We have suggested several new avenues to explore experimentally, including temperature

dependence, low excitation density, and, surface passivation. These studies will likely shed light on the mechanism of THz-PLQ in the low fluence regime. To understand the high fluence regime, modelling will be required due to nonlinear absorption and effects extreme carrier densities.

Chapter 6

Conclusion

Despite having been a major research focus for decades, new work on semiconductors such as GaAs and InP is still leading to new physics. While theories exist which are formally exact, complexity limits their predicatability and experiment is required as a guide. With the development of new tools, qualitatively new information can lead to new insight.

In the last several years, the technique of tilted-pulse-front optical rectification in lithium niobate has brought THz nonlinear optics to the optics bench. With our lithium niobate source, we have achieved peak electric fields of 230 kV/cm. This source has been used to study nonlinearities of transient states in semiconductors.

We have studied how these pulses can modulate photoluminescence in GaAs and InP. Modulation only occurs when the photoexcitation and THz pulse are simultaneously incident on the crystal. When transform limited photoexcitation pulses are used, PLQ is observed near the bandgap, PLE is observed for hot carriers at all carrier densities. However, quenching dominates, and there is an overall reduction in intensity.

We have discussed several possible mechanisms for the THz modulation of luminescence, 1) non-radiative recombination due to intervalley phonons, 2) suppressed diffusion into the substrate, enhancing surface recombination, due to intervalley scattering, and, 3) suppression of stimulated emission by intervalley scattering. Exploration of the low carrier density and low temperature regimes will shed light on which of these

mechanisms is the correct interpretation.

The intervalley phonon enhanced non-radiative recombination would be of interest to device engineers, and clarification is needed as to whether this occurs. Alternatively, the second mechanism, the enhancement of surface recombination, also needs clarification. The physics of interfaces is an important field in itself, and much of modern materials science is based on the devlopement of functionalized surfaces. This mechanism would represent a new tool to control optically excited distributions in real space, potentially acting as a unique probe of interface physics.

Perhaps the most interesting possibility would be if suppression of stimulated emission is the origin. Exploration of these effects at low temperature, could yield interesting results. The ability to modulate stimulated emission on picosecond timescales would present unique technological applications, and point to a broad range of novel systems to study THz modulation of luminescence.

The high excitation density results are still puzzling. Adjustment of the laser pulse compressor can result in integrated luminescence enhancement, and modification of the luminescence spectrum. It is unclear how any of the previously discussed models can explain the results in this regime. This behaviour may be difficult to understand, due to the extreme pump fluences, but better laser pulse characterization will be required to understand this regime.

As part of the bigger picture, this work fits in a community which aims to understand the nature of light-matter interactions from a fundamental level. Over the last several decades, the development of new technologies has resulted in a continually shifting paradigm of light-matter interactions, especially in the regime just picoseconds after photoexcitation. Intense THz pulse sources represent one such technology, helping to add new pieces to the puzzle. This work will help clarify our understanding of the ultrafast interactions which occur immediately after photoexcitation.

References

[1] T. H. Maiman. **Stimulated Optical Radiation in Ruby**. *Nature*, **187**(4736):493–494, 1960. [pg. 2]

[2] P. A. Franken, A. E. Hill, C. W. Peters, and G. Weinreich. **Generation of Optical Harmonics**. *Phys. Rev. Lett.*, **7**:118–119, Aug 1961. [pg. 2]

[3] S. Backus, Charles G. Durfee III, M. M. Murnane, and H. C. Kapteyn. **High power ultrafast lasers**. *Review of Scientific Instruments*, **69**(3):1207–1223, 1998. [pg. 2]

[4] T. J. Hammond, G. G. Brown, K. Taec Kim, D. M. Villeneuve, and P. B. Corkum. **Attosecond pulses measured from the attosecond lighthouse**. *Nat. Photon.*, **10**(3):171–175, Mar 2016. Letter. [pg. 2]

[5] F. H. Su, F. Blanchard, G. Sharma, L. Razzari, A. Ayesheshim, T. L. Cocker, L. V. Titova, T. Ozaki, J.-C. Kieffer, R. Morandotti, M. Reid, and F. A. Hegmann. **Terahertz pulse induced intervalley scattering in photoexcited GaAs**. *Optics Express*, **17**(12):9620, 2009. [pg. 2]

[6] P. U. Jepsen, D. G. Cooke, and M. Koch. **Terahertz spectroscopy and imaging Modern techniques and applications**. *Laser & Photonics Reviews*, **5**(1):124–166, 2011. [pg. 3]

[7] S. Keiber, S. Sederberg, A. Schwarz, M. Trubetskov, V. Pervak, F. Krausz, and N. Karpowicz. **Electro-optic sampling of near-infrared waveforms**. *Nature Photonics*, **10**(3):159–162, 2016. [pg. 3]

[8] M. C. Nuss, D. H. Auston, and F. Capasso. **Direct Subpicosecond Measurement of Carrier Mobility of Photoexcited Electrons in Gallium Arsenide**. *Physical Review Letters*, **58**(22):2355–2358, 1987. [pg. 3]

[9] R. Huber, F. Tauser, A. Brodschelm, M. Bichler, G. Abstreiter, and A. Leitenstorfer. **How many-particle interactions develop after ultrafast excitation of an electronhole plasma**. *Nature*, **414**(6861):286–289, 2001. [pg. 3, 72]

[10] R. A. Kaindl, M. A. Carnahan, D. Hägele, R. Lövenich, and D. S. Chemla. **Ultrafast terahertz probes of transient conducting and insulating phases in an electronhole gas**. *Nature*, **423**(6941):734–738, 2003. [pg. 4, 19, 72]

[11] O. Schubert, M. Hohenleutner, F. Langer, B. Urbanek, C. Lange, U. Huttner, D. Golde, T. Meier, M. Kira, S. W. Koch, and R. Huber. **Sub-cycle control of terahertz high-harmonic generation by dynamical Bloch oscillations**. *Nature Photonics*, **8**(2):119–123, 2014. [pg. 4]

[12] K.-L. Yeh, M. C. Hoffmann, J. Hebling, and Keith A. Nelson. **Generation of 10μJ ultrashort terahertz pulses by optical rectification**. *Applied Physics Letters*, **90**(17):171121, 2007. [pg. 4, 33]

[13] L. Razzari, F. H. Su, G. Sharma, F. Blanchard, A. Ayesheshim, H.-C. Bandulet, R. Morandotti, J.-C. Kieffer, T. Ozaki, M. Reid, and F. A. Hegmann. **Nonlinear ultrafast modulation of the optical absorption of intense few-cycle terahertz pulses in n -doped semiconductors**. *Physical Review B*, **79**(19):193204, 2009. [pg. 4, 22]

[14] T. Kampfrath, A. Sell, G. Klatt, A. Pashkin, S. Mährlein, T. Dekorsy, M. Wolf, M. Fiebig, A. Leitenstorfer, and R. Huber. **Coherent terahertz control of antiferromagnetic spin waves**. *Nature Photonics*, **5**(1):31–34, 2011. [pg. 4]

[15] C. Lange, T. Maag, M. Hohenleutner, S. Baierl, O. Schubert, E.R.J. Edwards, D. Bougeard, G. Woltersdorf, and R. Huber. **Extremely Nonperturbative Nonlinearities in GaAs Driven by Atomically**

Strong Terahertz Fields in Gold Metamaterials. *Physical Review Letters*, **113**(22):227401, 2014. [pg. 4, 44, 68]

[16] T. Kampfrath, K. Tanaka, and K. A. Nelson. **Resonant and nonresonant control over matter and light by intense terahertz transients**. *Nature Photonics*, **7**(9):680–690, 2013. [pg. 4]

[17] Charles Kittel. *Introduction to Solid State Physics*. John Wiley & Sons, Inc., New York, 6th edition, 1986. [pg. 9]

[18] Robert W. Boyd. *Nonlinear Optics, Third Edition*. Academic Press, 3rd edition, 2008. [pg. 9]

[19] E. Wigner and F. Seitz. **On the Constitution of Metallic Sodium**. *Physical Review*, **43**(10):804–810, 1933. [pg. 10]

[20] I. Saïdi, S. Ben Radhia, and K. Boujdaria. **Band parameters of GaAs, InAs, InP, and InSb in the 40-band kp model**. *Journal of Applied Physics*, **107**(4):043701, 2010. [pg. 10, 50]

[21] Timothy B. Boykin, Gerhard Klimeck, R. Chris Bowen, and Fabiano Oyafuso. **Diagonal parameter shifts due to nearest-neighbor displacements in empirical tight-binding theory**. *Phys. Rev. B*, **66**:125207, Sep 2002. [pg. 10]

[22] A. De and C. E. Pryor. **Predicted band structures of III-V semiconductors in the wurtzite phase**. *Physical Review B*, **81**(15):155210, 2010. [pg. 10]

[23] I. Vurgaftman, J. R. Meyer, and L. R. Ram-Mohan. **Band parameters for IIIV compound semiconductors and their alloys**. *Journal of Applied Physics*, **89**(11):5815–5875, 2001. [pg. 12]

[24] P. Würfel. **The chemical potential of radiation**. *Journal of Physics C: Solid State Physics*, **15**(18):3967, 1982. [pg. 14]

[25] D. S. Kim and P. Y. Yu. **Phonon temperature overshoot in GaAs excited by subpicosecond laser pulses**. *Physical Review Letters*, **64**(8):946–949, 1990. [pg. 14, 51]

[26] I. Pelant and J. Valenta. *Luminescence Spectroscopy of Semiconductors*. Luminescence Spectroscopy of Semiconductors. OUP Oxford, 2012. [pg. 15]

[27] W. Shockley and W. T. Read Jr. **Statistics of the Recombinations of Holes and Electrons**. *Physical Review*, **87**(5):835–842, 1952. [pg. 15]

[28] Mark Lundstrom. *Fundamentals of Carrier Transport*. Cambridge University Press, 2009. [pg. 17]

[29] S. Hunsche, H. Heesel, A. Ewertz, H. Kurz, and J. H. Collet. **Spectral-hole burning and carrier thermalization in GaAs at room temperature**. *Physical Review B*, **48**(24):17818, 1993. [pg. 18]

[30] M Feneberg, S. Osterburg, K. Lange, C. Lidig, B. Garke, R. Goldhahn, E. Richter, C. Netzel, M. D. Neumann, N. Esser, S. Fritze, H. Witte, J. Bläsing, A. Dadgar, and A. Krost. **Band gap renormalization and Burstein-Moss effect in silicon- and germanium-doped wurtzite GaN up to 10^{20} cm^3**. *Physical Review B*, **90**(7):075203, 2014. [pg. 18]

[31] A. Leitenstorfer, T. Elsaesser, F. Rossi, T. Kuhn, W. Klein, G. Boehm, G. Traenkle, and G. Weimann. **Coherent optical generation of nonequilibrium electrons studied via band-to-acceptor luminescence in GaAs**. *Physical Review B*, **53**(15):9876, 1996. [pg. 19, 53]

[32] Mark Fox. *Optical properties of solids*, **3**. Oxford university press, 2010. [pg. 19, 51]

[33] Mackillo Kira and Stephan W. Koch. *Semiconductor Quantum Optics*. Cambridge University Press, 2011. [pg. 19]

[34] J. Sjakste, N. Vast, M. Calandra, and F. Mauri. **Wannier interpolation of the electron-phonon matrix elements in polar semiconductors: Polar-optical coupling in GaAs**. *Physical Review B*, **92**(5):054307, 2015. [pg. 20]

[35] M. Bernardi, D. Vigil-Fowler, C. S. Ong, J. B. Neaton, and S. G. Louie. **Ab initio study of hot electrons in GaAs**. *Proceedings of the National Academy of Sciences of the United States of America*, **112**(17):5291–5296, 2015. [pg. 20]

[36] J. A. Kash, J. C. Tsang, and J. M. Hvam. **Subpicosecond time-resolved Raman spectroscopy of LO phonons in GaAs**. *Physical review letters*, **54**(19):2151, 1985. [pg. 20]

[37] A. Leitenstorfer, S. Hunsche, J. Shah, M. C. Nuss, and W. H. Knox. **Femtosecond high-field transport in compound semiconductors**. *Physical Review B*, **61**(24):16642–16652, 2000. [pg. 22, 53]

[38] G. Klatt, F. Hilser, W. Qiao, M. Beck, R. Gebs, A. Bartels, K. Huska, U. Lemmer, G. Bastian, M.B. Johnston, M. Fischer, J. Faist, and T. Dekorsy. **Terahertz emission from lateral photo-Dember currents**. *Optics Express*, **18**(5):4939, 2010. [pg. 22, 70]

[39] M. Reid, I. V. Cravetchi, and R. Fedosejevs. **Terahertz radiation and second-harmonic generation from InAs: Bulk versus surface electric-field-induced contributions**. *Physical Review B*, **72**(3):035201, 2005. [pg. 22, 70]

[40] M. C. Beard, G. M. Turner, and C. A. Schmuttenmaer. **Transient photoconductivity in GaAs as measured by time-resolved terahertz spectroscopy**. *Physical Review B*, **62**(23):15764, 2000. [pg. 23]

[41] M. Beaudoin, A. J. G. DeVries, S. R. Johnson, H. Laman, and T. Tiedje. **Optical absorption edge of semi-insulating GaAs and InP at high temperatures**. *Applied physics letters*, **70**(26):3540–3542, 1997. [pg. 25]

[42] J. K. Katahara and H. W. Hillhouse. **Quasi-Fermi level splitting and sub-bandgap absorptivity from semiconductor photoluminescence**. *Journal of Applied Physics*, **116**(17):173504, 2014. [pg. 25]

[43] J. H. Collet, W. W. Rühle, M. Pugnet, K. Leo, and A. Million. **Electron-hole plasma dynamics in CdTe in the picosecond regime**. *Phys. Rev. B*, **40**(18):12296–12303, Dec 1989. [pg. 25, 51]

[44] T. Brabec, Ch. Spielmann, P. F. Curley, and F. Krausz. **Kerr lens mode locking**. *Optics Letters*, **17**(18):1292, 1992. [pg. 28]

[45] A. M. Dunlop, W. J. Firth, and E. M. Wright. **Master equation for spatio-temporal beam propagation and Kerr lens mode-locking**. *Optics Communications*, **138**(1):211–226, 1997. [pg. 28]

[46] B. Proctor, E. Westwig, and F. Wise. **Characterization of a Kerr-lens mode-locked Ti:sapphire laser with positive group-velocity dispersion**. *Optics Letters*, **18**(19):1654, 1993. [pg. 28]

[47] Liu Hua-Gang, Hu Ming-Lie, Song You-Jian, Li Yan-Feng, Chai Lu, and Wang Ching-Yue. **Operation of Kerr-lens mode-locked Ti:sapphire laser in the non-soliton regime**. *Chinese Physics B*, **19**(1):014215–6, 2010. [pg. 28]

[48] J. V. Rudd, G. Korn, S. Kane, J. Squier, G. Mourou, and P. Bado. **Chirped-pulse amplification of 55-fs pulses at a 1-kHz repetition rate in a Ti:Al_2O_3 regenerative amplifier**. *Optics Letters*, **18**(23):2044, 1993. [pg. 28]

[49] Andrew Marc Weiner. *Ultrafast optics*. Wiley series in pure and applied optics. Wiley, 2009. [pg. 31]

[50] Rick Trebino, Kenneth W. DeLong, David N. Fittinghoff, John N. Sweetser, Marco A. Krumbügel, Bruce A. Richman, and Daniel J. Kane. **Measuring ultrashort laser pulses in the time-frequency domain using frequency-resolved optical gating**. *Review of Scientific Instruments*, **68**(9):3277–3295, 1997. [pg. 31]

[51] Daniel J. Kane. **Principal components generalized projections: a review [Invited]**. *JOSA B*, **25**(6):A120–A132, 2008. [pg. 32]

[52] Patrick O'Shea, Mark Kimmel, Xun Gu, and Rick Trebino. **Highly simplified device for ultrashort-pulse measurement**. *Optics Letters*, **26**(12):932, 2001. [pg. 32]

[53] Masaya Nagai, Mukesh Jewariya, Yuki Ichikawa, Hideyuki Ohtake, Toshiharu Sugiura, Yuzuru Uehara, and Koichiro Tanaka. **Broadband and high power terahertz pulse generation beyond excitation bandwidth limitation via $\chi^{(2)}$ cascaded processes in $LiNbO_3$**. *Optics Express*, **17**(14):11543, 2009. [pg. 33, 41]

[54] Koustuban Ravi, Wenqian Ronny Huang, Sergio Carbajo, Emilio A. Nanni, Damian N. Schimpf, Erich P. Ippen, and Franz. X. Kärtner. **Theory of terahertz generation by optical rectification using tilted-pulse-fronts**. *Optics Express*, **23**(4):5253, 2015. [pg. 33, 41]

[55] J. A. Fülöp, L. Pálfalvi, G. Almási, and J. Hebling. **Design of high-energy terahertz sources based on optical rectification**. *Optics Express*, **18**(12):12311, 2010. [pg. 33, 35]

[56] Michael I. Bakunov and Sergey B. Bodrov. **Terahertz generation with tilted-front laser pulses in a contact-grating scheme**. *Journal of the Optical Society of America B*, **31**(11):2549, 2014. [pg. 33]

[57] T. E. Stevens, J. K. Wahlstrand, J. Kuhl, and R. Merlin. **Cherenkov Radiation at Speeds Below the Light Threshold: Phonon-Assisted Phase Matching**. *Science*, **291**(5504):627–630, 2001. [pg. 34]

[58] Maksim Kunitski, Martin Richter, Mark D. Thomson, Arno Vredenborg, Jian Wu, Till Jahnke, Markus Schöffler, Horst Schmidt-Böcking, Hartmut G. Roskos, and Reinhard Dörner. **Optimization of single-cycle terahertz generation in LiNbO_3 for sub-50 femtosecond pump pulses**. *Optics Express*, **21**(6):6826, 2013. [pg. 35]

[59] H. Hirori, A. Doi, F. Blanchard, and K. Tanaka. **Single-cycle terahertz pulses with amplitudes exceeding 1 MV/cm generated by optical rectification in LiNbO3**. *Applied Physics Letters*, **98**(9):091106, 2011. [pg. 35, 37]

[60] I.z. Kozma, G. Almsi, and J. Hebling. **Geometrical optical modeling of femtosecond setups having angular dispersion**. *Applied Physics B: Lasers & Optics*, **76**(3):257, 2003. [pg. 35]

[61] Zhenyou Wang. *Ultrafast imaging of terahertz waves*. PhD thesis, University of Alberta, 2013. [pg. 36]

[62] A. K. Ayesheshim. *High-power Terahertz Pulse Generation and Nonlinear Terahertz Carrier Dynamics in Semiconductors*. PhD thesis, University of Alberta, 2015. [pg. 37, 60, 70]

[63] Yun-Shik Lee. *Principles of Terahertz Science and Technology*. Springer Publishing Company, Incorporated, 1st edition, 2008. [pg. 37]

[64] F. Blanchard, X. Ropagnol, H. Hafez, H. Razavipour, M. Bolduc, R. Morandotti, T. Ozaki, and D. G. Cooke. **Effect of extreme pump pulse reshaping on intense terahertz emission in lithium niobate at multimilliJoule pump energies**. *Optics Letters*, **39**(15):4333, 2014. [pg. 41]

[65] G. Sharma, I. Al-Naib, H. Hafez, R. Morandotti, D. G. Cooke, and T. Ozaki. **Carrier density dependence of the nonlinear absorption of intense THz radiation in GaAs**. *Optics Express*, **20**(16):18016, 2012. [pg. 43, 70]

[66] Martin van Exter, Ch. Fattinger, and D. Grischkowsky. **Terahertz time-domain spectroscopy of water vapor**. *Optics Letters*, **14**(20):1128, 1989. [pg. 44]

[67] Jingle Liu, Gurpreet Kaur, and X.-C. Zhang. **Photoluminescence quenching dynamics in cadmium telluride and gallium arsenide induced by ultrashort terahertz pulse**. *Applied Physics Letters*, **97**(11):111103, 2010. [pg. 48, 49, 55, 69]

[68] Zheng Chu, Jinsong Liu, and Jingle Liu. **Study of THz-wave-induced photoluminescence quenching in GaAs and CdTe**. *Applied Physics B*, **109**(1):113–119, 2012. [pg. 48, 69]

[69] D. J. Ashen, P. J. Dean, D. T. J. Hurle, J. B. Mullin, A. M. White, and P. D. Greene. **The incorporation and characterisation of acceptors in epitaxial GaAs**. *Journal of Physics and Chemistry of Solids*, **36**(10):1041–1053, 1975. [pg. 51]

[70] Bruno Ullrich, Akhilesh K. Singh, Puspendu Barik, Haowen Xi, and Mithun Bhowmick. **Inherent photoluminescence Stokes shift in GaAs**. *Optics Letters*, **40**(11):2580, 2015. [pg. 51]

[71] O. Madelung. *Semiconductors Basic Data*. Springer Berlin Heidelberg, 2012. [pg. 51]

[72] P. G. Klemens. **Anharmonic Decay of Optical Phonons**. *Physical Review*, **148**(2):845–848, 1966. [pg. 53]

[73] Hani Hamzeh and Frédéric Aniel. **Monte Carlo study of phonon dynamics in III-V compounds**. *Journal of Applied Physics*, **109**(6):063511, 2011. [pg. 53]

[74] Raphael Clady, Murad J. Y. Tayebjee, Pasquale Aliberti, Dirk König, Nicholas John Ekins-Daukes, Gavin J. Conibeer, Timothy W. Schmidt, and Martin A. Green. **Interplay between the hot phonon effect and intervalley scattering on the cooling rate of hot carriers in GaAs and InP**. *Progress in Photovoltaics: Research and Applications*, **20**(1):82–92, 2012. [pg. 55]

[75] C. J. Hwang. **Quantum efficiency and radiative lifetime of the band-to-band recombination in heavily doped n-type GaAs**. *Physical Review B*, **6**(4):1355, 1972. [pg. 55]

[76] U. Strauss, W. W. Rühle, and K. Köhler. **Auger recombination in intrinsic GaAs**. *Applied Physics Letters*, **62**(1):55–57, 1993. [pg. 57, 72]

[77] Jacques I. Pankove. *Optical Processes in Semiconductors*. Courier Corporation, 1971. [pg. 58, 71]

[78] J. Shah, C. Lin, R. F. Leheny, and A. E. DiGiovanni. **Pump wavelength dependence of hot electron temperature in GaAs**. *Solid State Communications*, **18**(4):487–489, 1976. [pg. 58, 71]

[79] Krzysztof Iwaszczuk, Maksim Zalkovskij, Andrew C. Strikwerda, and Peter U. Jepsen. **Nitrogen plasma formation through terahertz-induced ultrafast electron field emission**. *Optica*, **2**(2):116, 2015. [pg. 60]

[80] J. Lloyd-Hughes, S. K. E. Merchant, L. Fu, H. H. Tan, C. Jagadish, E. Castro-Camus, and M. B. Johnston. **Influence of surface passivation on ultrafast carrier dynamics and terahertz radiation generation in GaAs**. *Applied Physics Letters*, **89**(23):232102, 2006. [pg. 60, 70]

[81] K. Shinokita, H. Hirori, K. Tanaka, T. Mochizuki, C. Kim, H. Akiyama, L. N. Pfeiffer, and K. W. West. **Terahertz-Induced Optical Emission of Photoexcited Undoped GaAs Quantum Wells**. *Physical Review Letters*, **111**(6), 2013. [pg. 68]

[82] W. D. Rice, J. Kono, S. Zybell, S. Winnerl, J. Bhattacharyya, H. Schneider, M. Helm, B. Ewers, A. Chernikov, M. Koch, S. Chatterjee, G. Khitrova, H. M. Gibbs, L. Schneebeli, B. Breddermann, M. Kira, and S. W. Koch. **Observation of Forbidden Exciton Transitions Mediated by Coulomb Interactions in Photoexcited Semiconductor Quantum Wells**. *Physical Review Letters*, **110**(13), 2013. [pg. 68]

[83] Fabio Novelli, Daniele Fausti, Francesca Giusti, Fulvio Parmigiani, and Matthias Hoffmann. **Mixed regime of light-matter interaction revealed by phase sensitive measurements of the dynamical Franz-Keldysh effect**. *Scientific Reports*, **3**, 2013. [pg. 69]

[84] M. Yao, T. Watanabe, P. K. Schelling, P. Keblinski, D. G. Cahill, and S. R. Phillpot. **Phonon-defect scattering in doped silicon by molecular dynamics simulation**. *Journal of Applied Physics*, **104**(2):024905, 2008. [pg. 69]

[85] A. Lohner, M. Woerner, T. Elsaesser, and W. Kaiser. **Picosecond capture of photoexcited holes by shallow acceptors in p-type GaAs**. *Physical Review Letters*, **68**(26):3920–3923, 1992. [pg. 69]

[86] V.N. Abakumov, V.I. Perel, and I.N. Yassievich. *Nonradiative Recombination in Semiconductors*. Modern Problems in Condensed Matter Sciences. North-Holland, 1991. [pg. 69]

[87] P. C. M. Christianen and H. J. A. Bluyssen. **The effect of stimulated emission on the cooling rate of hot carriers in GaAs**. *Physica B: Condensed Matter*, **204**(1):325–331, 1995. [pg. 71]

[88] Jagdeep Shah, Benoit Deveaud, T. C. Damen, W. T. Tsang, A. C. Gossard, and P. Lugli. **Determination of intervalley scattering rates in GaAs by subpicosecond luminescence spectroscopy**. *Physical review letters*, **59**(19):2222, 1987. [pg. 71]

[89] W. Sritrakool, V. Sa-Yakanit, and H. R. Glyde. **Absorption near band edges in heavily doped GaAs**. *Physical Review B*, **32**(2):1090, 1985. [pg. 72]

[90] W. Z. Lin, L. G. Fujimoto, E. P. Ippen, and R. A. Logan. **Femtosecond carrier dynamics in GaAs**. *Applied Physics Letters*, **50**(3):124–126, 1987. [pg. 72]

[91] Muneaki Hase, Masayuki Katsuragawa, Anca Monia Constantinescu, and Hrvoje Petek. **Coherent phonon-induced optical modulation in semiconductors at terahertz frequencies**. *New Journal of Physics*, **15**(5):055018, 2013. [pg. 72]

[92] Jun'ichi Kanasaki, Hiroshi Tanimura, and Katsumi Tanimura. **Imaging Energy-, Momentum-, and Time-Resolved Distributions of Photoinjected Hot Electrons in GaAs**. *Phys. Rev. Lett.*, **113**:237401, Dec 2014. [pg. 72]